University of Maribor
Faculty of Energy Technology

# Journal of ENERGY TECHNOLOGY


Volume 10 / Issue 3
OCTOBER 2017
www.fe.um.si/en/jet.html

# Journal of ENERGY TECHNOLOGY

**VOLUME 10 / Issue 3**

Revija Journal of Energy Technology (JET) je indeksirana v bazah INSPEC© in Proquest's Technology Research Database.

The Journal of Energy Technology (JET) is indexed and abstracted in database INSPEC© and Proquest's Technology Research Database.

# JOURNAL OF ENERGY TECHNOLOGY

**Izhajanje revije / PUBLISHING**

Revija izhaja štirikrat letno v nakladi 150 izvodov. Članki so dostopni na spletni strani revije - www.fe.um.si/si/jet.html / The journal is published four times a year. Articles are available at the journal's home page - www.fe.um.si/en/jet.html.
Cena posameznega izvoda revije (brez DDV) / Price per issue (VAT not included in price): 50,00 EUR
Informacije o naročninah / Subscription information: http://www.fe.um.si/en/jet/subscriptions.html



Izdajanje revije JET finančno podpira Javna agencija za raziskovalno dejavnost Republike Slovenije iz sredstev državnega proračuna iz naslova razpisa za sofinanciranje domačih znanstvenih periodičnih publikacij / The Journal of Energy Technology is co-financed by the Slovenian Research Agency.

## *Spoštovani bralci revije Journal of energy technology (JET)*

V prihodnjih desetletjih bomo priča revolucionarnim premikom na področju energetike. Predvidevajo se spremembe na področju proizvodnje električne in toplotne energije, kakor tudi v transportu in ostalih sektorjih energetike. Delež obnovljivih virov in alternativnih sistemov bo mnogo večji kot doslej. V novih tehnologijah mnogo tehničnih detajlov še ni dovršenih; novi materiali so v razvoju, smo v pričakovanju izvirnih idej. V številnih primerih ideje, ki so največkrat zelo preproste, predstavijo mladi izumitelji, nadarjeni študenti, zato je zelo pomembno, da šolski sistem omogoči nadarjenim študentom in njihovim mentorjem kreativno delo.

Zelo rad komuniciram s študenti, ki izžarevajo strast do raziskovalnega dela ali razvoja določene ideje. V tej številki revije je predstavljena prav takšna skupina, ki že nekaj časa uspešno razvija idejo razvoja dirkalnega avtomobila. Pri njihovem nadaljnjem delu jim želim veliko uspeha.

Jurij AVSEC
odgovorni urednik revije JET

## *Dear Readers of the Journal of Energy Technology (JET)*

Revolutions in the field of energy and energy technology are certain in the coming decades. It is anticipated that major changes will occur in the areas of electricity and heat production, as well as in transport and other energy sectors. Renewable resources and alternative systems will contribute a much larger share than at present. Many technical details of the new technologies have not yet been solved: they are waiting for original ideas and new materials. In many cases, the original ideas, which are often very simple, are presented by young inventors, talented students, and their colleagues. Therefore, it is vital that the school system enable talented students to develop their ideas, of course in connection with the mentors.

I like to communicate with such students from whom a passion for research work or the development of a certain idea radiates. In this issue of the magazine, this group is represented; for quite some time, they have successfully developed the idea of developing a racing car. In their further work, I wish them much success.

Jurij AVSEC
Editor-in-chief of JET

# *Table of Contents / Kazalo*

Journal of Energy Technology

JET Volume 10 (2017) p.p. 11-23
Issue 3, October 2017
Type of article 1.01
www.fe.um.si/en/jet.html

# THE OPTIMIZATION OF A RACE CAR INTAKE SYSTEM

# OPTIMIZACIJA SESALNEGA SISTEMA DIRKALNIKA

Luka Lešnik [1✉], Nejc Mlakar[1], Ignacijo Biluš[1], Breda Kegl[1]

**Keywords:** pressure fluctuation, engine intake design, optimization, air trumpets

## Abstract

This paper deals with the optimization of a race car intake system in order to increase engine power output. The goal of optimization was to test how different lengths of intake trumpet influence air mass flow, pressure fluctuations and, consequently, the obtained engine-rated power and torque. Six trumpet lengths were tested using the 1-D AVL BOOST simulation program. The obtained numerical results of engine-rated power and torque were compared with the information obtained from the engine's manufacturer.

The results of optimization indicate that the length of the intake trumpet significantly influences pressure fluctuation in the test engine intake system. At specific trumpet lengths, pressure fluctuation can help to increase air mass flow per engine cycle, which consequently influences engine-rated power and torque. It was found that shorter intake trumpets have an influence on a higher engine-rated power when operating at higher engine rotational speeds. Longer trumpets increase engine-rated torque at lower engine rotational speeds but decrease engine power at higher speeds. For the needs of competition, high peak engine power is desired, so the trumpets with 60 mm length were selected as optimal, because they have the highest peak engine power output at the desired engine speed.

✉ Corresponding author: Luka Lešnik, Phd. Tel.: +386 2 220 7734, Mailing address: University of Maribor, Faculty of Mechanical Engineering, Smetanova ulica 17, 2000 Maribor, Slovenia, E-mail address: luka.lesnik@um.si

[1] University of Maribor, Faculty of Mechanical Engineering, Internal combustion engines laboratory, Smetanova ulica 17, 2000 Maribor, Slovenia

## Povzetek

Predstavljeni članek obravnava optimizacijo sesalnega sistema motorja z namenom izboljšanja njegove moči. Cilj optimizacije je bil raziskati vpliv dolžine vstopnih cevi (tub) sesalnega sistema na masni pretok zraka, tlačna nihanja, moč in navor motorja. V ta namen smo testirali šest dolžin vstopnih cevi z uporabo 1-D numeričnega programa AVL BOOST. Dobljeni rezultati simulacij so bili primerjani s podatki pridobljeni s strani proizvajalca motorja.

Rezultati optimizacije kažejo, da dolžina vstopne cevi pomembno vpliva na tlačna nihanja v sesalnem sistemu testnega motorja. Pri določeni dolžini lahko tlačna nihanja pomagajo izboljšati masni pretok zraka, kar nadaljnjo vpliva na povečanje moči in navora motorja. Iz rezultatov smo spoznali, da krajše dolžine cevi vplivajo na povečanje moči in navora motorja pri višjih vrtljajih. Z uporabo daljših cevi vplivamo na povečanje zmogljivosti motorja pri nižjih vrtljajih in zmanjšanje njegove zmogljivosti pri višjih vrtljajih. Za potrebe tekmovanja potrebujemo večjo moč pri visokih vrtljajih motorja zato smo kot optimalno izbrali cev z dolžino 60 mm.

## 1 INTRODUCTION

The air intake system of an engine is a major component responsible for delivering the required amounts of air into the engine combustion chamber. In engines with carburetors, intake trumpets can easily be replaced without any other modifications on the engine or its components. Engine component manufacturers offer several types of intake trumpets which differ in their length and diameter. The diameter of trumpet must fit the carburetor diameter used, so the only possible variable is the trumpet length. The length of the intake trumpet influences the airflow inside it, which is highly unsteady. The pressure fluctuation or wave action inside the trumpet consist of resonant acoustic behaviour and the so-called inertial ram effect of air. These were studied experimentally by several authors in the early stages of engine development, [1-3]. Based on experimental results, it was concluded that inertial and acoustic resonance effects could contribute to increases in engine peak performance. The importance of the ram effect and acoustic resonance effect on the volumetric efficiency of the engine is highly influenced by engine speed and intake system characteristics.

In recent years, experimental testing has been replaced using numerical simulations (NS), which are used in several research and engineering fields. Jošt et al., [4], used numerical simulations for improving Kaplan turbine efficiency prediction, Iljaž et al., [5], used NS for the optimization of the SAE formula rear wing while Harih et al., [6-7], used numerical methods in biomechanics. The most commonly used numerical models for analyzing engine intake systems are one-dimensional models, [8]. They can simultaneously take into account the unsteady flow in intake pipes and unsteady air flow through engine valves.

Numerical simulations can be made using commercial or ''in-house'' codes. Cottyn, [9], used the AVL BOOST simulation program to calculate and study intake the wave dynamics of a single-cylinder Formula 1 (F1) engine. Harrison et al., [10], made a detailed study on the acoustics of the intake system of a single cylinder F1 car. Based on experimental results they derived an acoustic and simple model of the inertia ram effect which allowed them to study both acoustic oscillations and ram effects at different engine speeds. Their conclusions are similar to those made from experimental work in [1-3]. The ram effect has very little or no influence on volumetric efficiency at the lower engine speed of an F1 engine. At higher engine speeds, it can have a strong contribution to the air intake process. At lower engine speeds, acoustic resonance effects have a

major influence on the air intake process. Yang et al., [11], used GT-Power software to perform an optimization of the intake system; intake manifold diameters and lengths were used as variables. The results of optimization show that the performance of the 1L four cylinders, naturally aspirated SI engine clearly improves with optimal intake system design.

For many engine intake systems, optimization is focused on engines with specific limitations. Sayyed, [12], and Vichi et al., [13], optimize the intake system geometry of a Formula Student, single-cylinder engine with the goal of increasing engine performance. Several different designs of the Venturi orifice were tested in [12]. The optimal design of selected intake ventured provides the air flow with the lowest pressure drop in the venture orifice. The authors in [13] tested the variable geometry intake plenum designs. The aim of the variable geometry was to provide the optimal intake geometry for different tests of the Formula SAE competition. It was concluded that innovative intake system design could enhance engine performance in specific tests of competition. The optimization of a Formula SAE race car engine was also performed in [14]. The optimization of a four-cylinder, naturally aspirated SI engine was done using 3D CFD code AVL FIRE. The selected optimal intake shape ensures equal loading of the air-fuel mixture to all the cylinders and consequently increases engine power.

In the present paper, the optimal intake system design of a four-cylinder race car engine was determined using the AVL BOOST v2013.2 computational program. The objective of intake optimization was the peak engine power at 5750 engine rotations per minute. The model of the race car engine was made in the program, and the results of engine power and torque from the engine manufacturer were validated. After model validation, several different lengths of engine intake trumpets were tested numerically. The optimal length of intake trumpet provides approximately 7% more engine power in comparison to less optimal trumpet lengths.

## 2 ENGINE MODEL

The model of the test engine was made in the AVL BOOST computational program. The specifications of the model are presented in Table 1.

***Table 1:*** *Engine specifications*

| | |
|---|---|
| Engine type | 182 AB 1AA 01 |
| Gas exchange | Naturally aspirated |
| Number of cylinders | 4 |
| Bore [mm] | 86.4 |
| Stroke [mm] | 67.4 |
| Compression ratio | 10.15 |
| Total displacement [$cm^3$] | 1584 |
| IVO/IVC (°ATDC) | 356/574 |
| EVO/EVC (°ATDC) | 144/362 |

The engine is equipped with two DHLA type Dellorto carburetors with 40mm diameter and 32mm venturi (choke) diameter. The model of the test engine made in the BOOST program is presented in Figure 1.

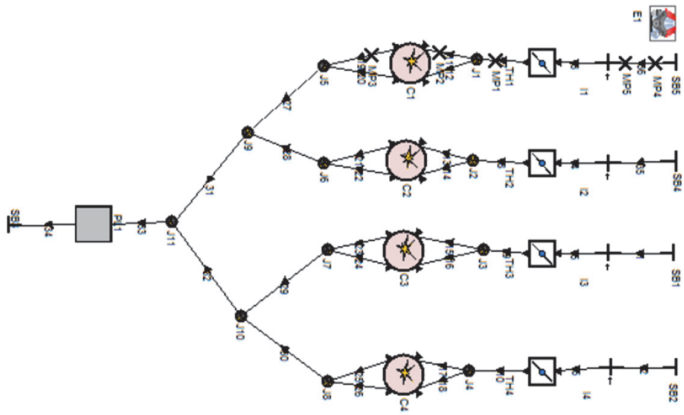

***Figure 1:*** *Engine model in BOOST*

To analyze pressure fluctuation in the intake system, four measurement points were placed in a virtual model of the test engine. The positions of the measurement points is schematically presented in Figure 2.

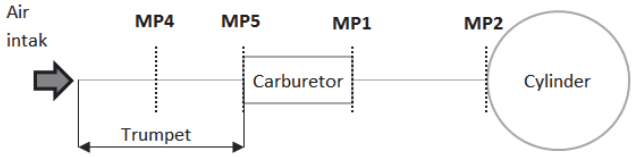


***Figure 2:*** *Schematic of intake system*

Measuring point MP2 was placed in the intake port (before the valve); MP1 was placed after the carburetor. MP4 and MP5 were placed in the centre and the end of the inlet trumpet, respectively.

Air with 25 °C and 1 bar of atmospheric pressure was used as a boundary condition at the intake side. At the exhaust side, a temperature of 250 °C and 1 bar of atmospheric pressure were used. The proper fuel mass flow was regulated with air-fuel equivalence ratio λ, which was set to 1.

# 3 GOVERNING EQUATIONS

The following governing equation can be written for the engine combustion chamber. The mass conservation equation can be written as:

$$dm = dm_I - dm_E + dm_f - dm_{BB} \tag{3.1}$$

Where $m$ is a mass on air/fuel mixture inside the combustion chamber, $m_I$ is mass of fresh mixture entering combustion chamber, $m_E$ is the mass of exhaust gasses exiting the combustion chamber, $m_f$ is the injected fuel mass, and $m_{BB}$ the mass of mixture blow-by.

The energy conservation equation for the engine combustion chamber can be written using Equation (3.2):

$$dU = dQ - p \cdot dV + dH \tag{3.2}$$

Where $dU$ stands for change of total energy, $dQ$ is the amount of heat transferred to the mixture inside the combustion chamber, $p$ is the pressure, $V$ current combustion chamber volume and $dH$ change of mixture enthalpy. The amount of heat in the combustion chamber transferred to mixture can be divided on heat release during combustion $dQ_c$ and heat losses through the chamber walls $dQ_w$.

$$dQ = dQ_c - dQ_w \tag{3.3}$$

The total heat released during the combustion process can be calculated using different combustion models. In the presented work, the Vibe combustion model was used for its calculation. Only a brief description of the combustion model used is in the following section. For a detailed description of the model, please refer to [15].

$$\frac{\frac{dQ_c}{Q}}{d\alpha} = \frac{a}{\Delta\alpha_c} \cdot (m+1) \cdot y^m \cdot e^{-a \cdot y^{(m+1)}} \tag{3.4}$$

$$y = \frac{\alpha - \alpha_{id}}{\Delta\alpha_c} \tag{3.5}$$

where $Q$ is total fuel heat input, $\alpha$ is crank angle, $a$ is Vibe parameter and $m$ shape parameter. Vibe and shape parameters were determined based on recommendations of AVL support for specific engine types and operating regimes (engine speeds).

# 4 RESULTS

The influence of intake trumpet length on a four-cylinder naturally aspirated SI engine was tested numerically. First, the accuracy of the numerical engine model was validated with the results of engine-rated power and torque provided by the engine manufacturer. The engine was equipped with 30-mm trumpets. The results of engine model validation are presented in Figure 3.

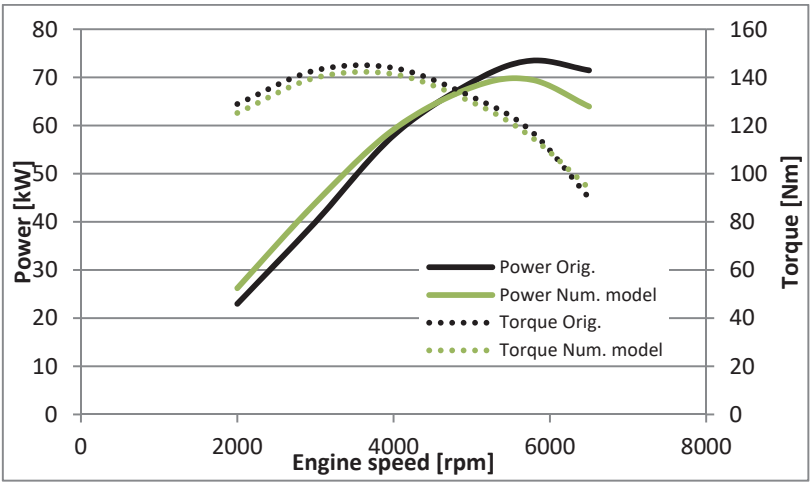


***Figure 3:*** *Results of engine model validation*

The results presented in Figure 3 show good agreement between the numerical model (Power/Torque Num. model) and the original (Power/torque Orig.) results of test engine-rated power and torque. The maximal differenced between engine-rated power and torque are in the range of 10%; average differences are in the range of 5%. This accuracy of test model enables using it for the numerical testing of trumpet length influence on engine characteristics. The following Figure 4-6 presents the numerical results of engine rated-power, torque, and airflow per cycle using different trumpet lengths.

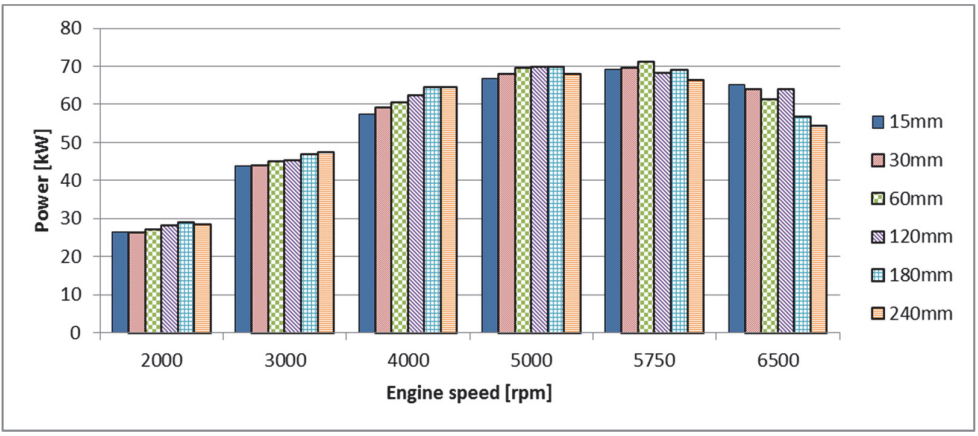


***Figure 4:*** *Numerical results of engine-rated power with different trumpet lengths*

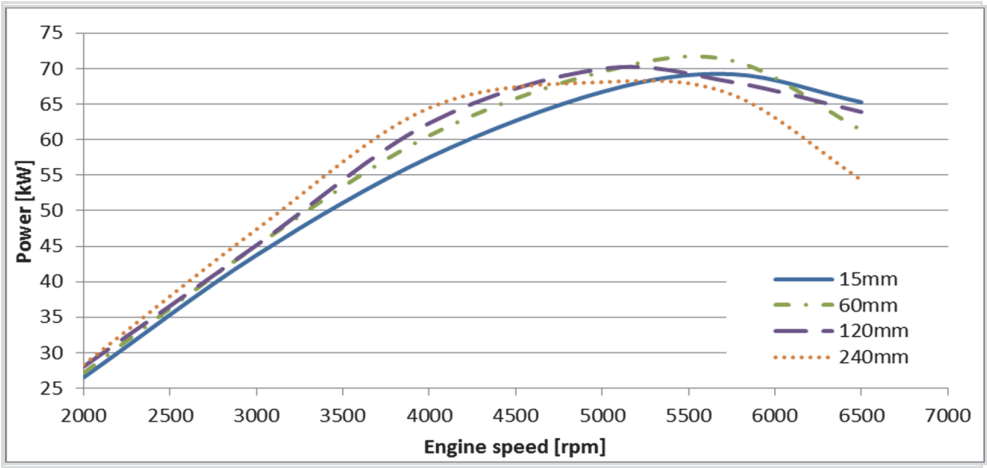


***Figure 5:*** *Numerical results of engine-rated power at selected trumpet lengths*

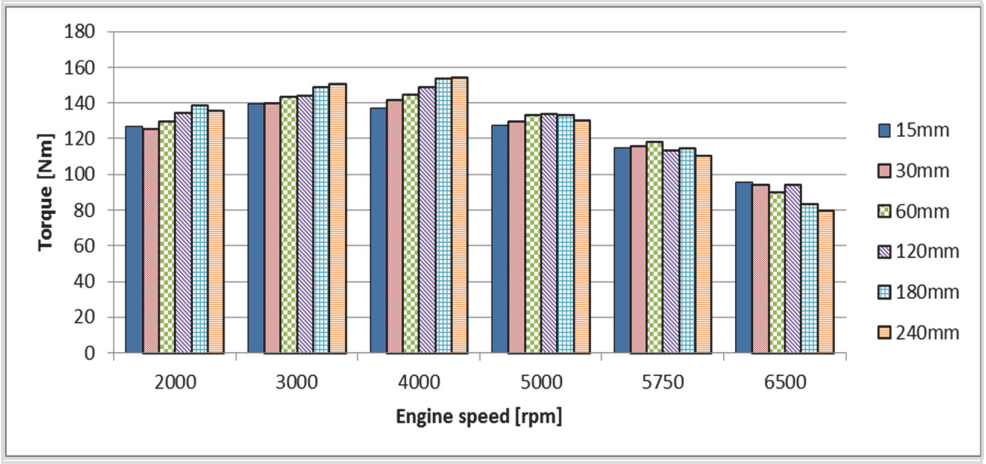


***Figure 6:*** *Numerical results of engine-rated torque with different trumpet lengths*

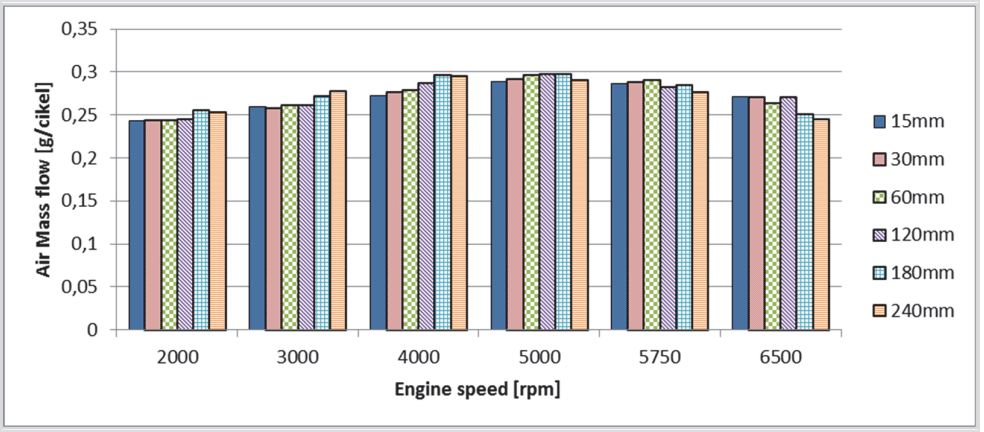


***Figure 7:*** *Numerical results of engine airflow per cycle with different trumpet lengths*

The results of the influence of trumpet length on engine-rated power are presented in Figures 4 and 5. It can be seen that longer trumpet lengths influence higher engine power up to 4000 rpm. At 5000 rpm, almost identical engine power was obtained when using 60-mm, 120-mm, and 180-mm long trumpets. At an engine speed of maximal power (5750 rpm), maximal engine power was obtained using the 60-mm long trumpet. At the highest engine speed (6500 rpm), maximal engine power was obtained with the shortest, 15-mm long trumpet. Maximal power output throughout engine operating range was obtained using 120-mm long trumpets, Figure 5.

The trumpet length also influences the engine-rated torque presented in Figure 6. The longer trumpets increase engine-rated torque at lower engine speeds. At an engine speed of maximal torque (4000 rpm), the maximal engine torque was obtained using 180-mm or 240-mm long trumpets. At 5750 rpm (engine speed of maximal power), the highest torque was obtained using a 60-mm long trumpet. At the highest engine speed, maximal torque was obtained using a 15-mm long trumpet.

The differences in engine-rated power and torque are a consequence of different air mass flows at different trumpet lengths presented in Figure 7. The highest air mass flow at 4000 rpm was obtained using a 180-mm long trumpet, while at 5750 rpm, a 60-mm long trumpet provides maximal air flow per engine cycle. Different lengths of trumpets influence the air pressure fluctuation in the intake system which further influence the air mass flows. Pressure fluctuations in the intake system for 60-mm and 240-mm long trumpets at 4000 and 5750 rpm are presented in Figures 8-11.

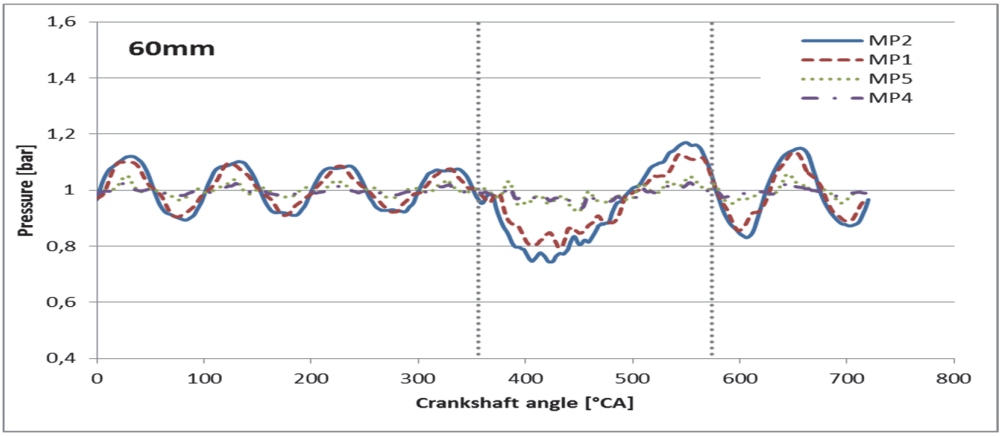


***Figure 8:*** *Pressure fluctuation in MP at 4000 rpm (60-mm trumpet)*

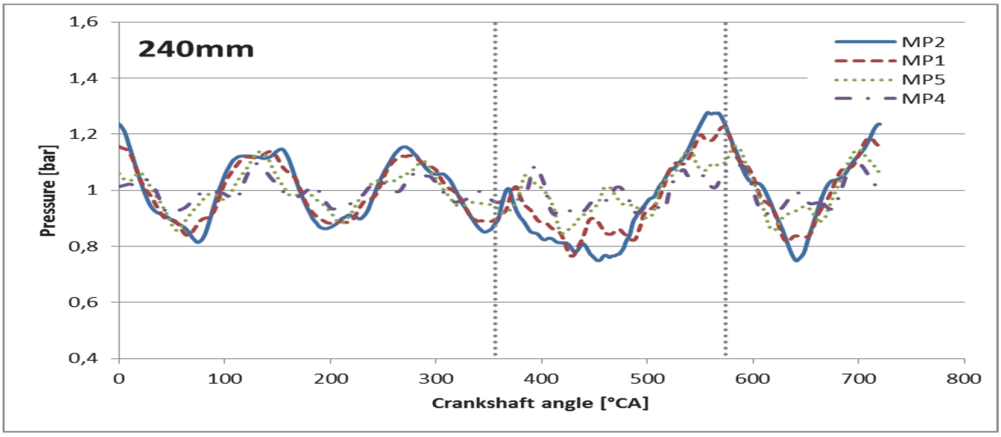


***Figure 9:*** *Pressure fluctuation in MP at 4000 rpm (240-mm trumpet)*

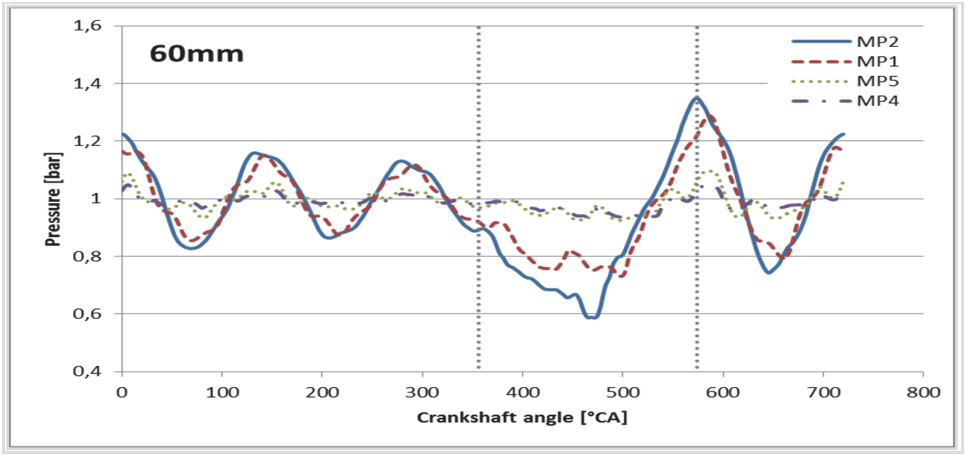


***Figure 10:*** *Pressure fluctuation in MP at 5750 rpm (60-mm trumpet)*

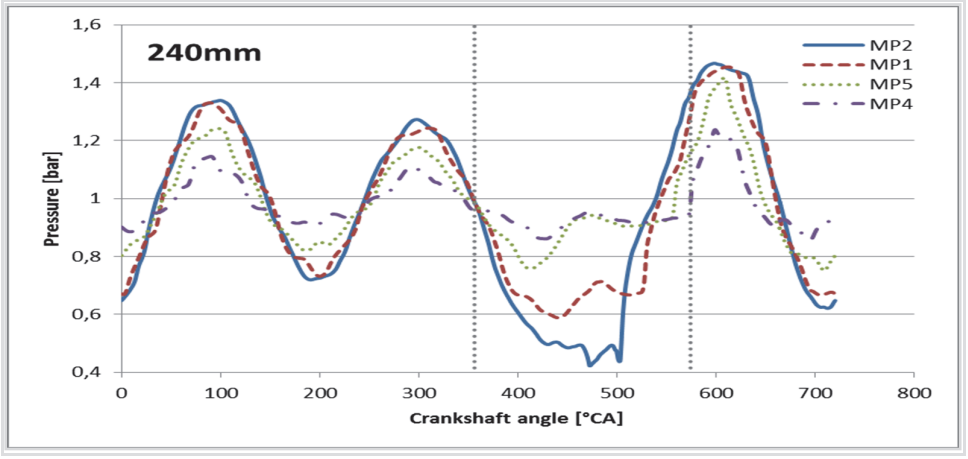


***Figure 11:*** *Pressure fluctuation in MP at 5750 rpm (240-mm trumpet)*

The results of pressure fluctuation in the inlet system are presented in Figures 8-11. Lower amplitude pressure fluctuations with higher frequency before intake valve opening were obtained using a 60-mm long trumpet at 4000 rpm. Higher amplitudes of pressure fluctuation at 5750 rpm were also obtained when using a 240-mm trumpet. At the moment of intake valve opening the pressure inside intake system drops because of the engine air suction. The maximal pressure drop at 4000 rpm is similar for both trumpet lengths and is approximately 0.25 bar below atmospheric pressure. The length of trumpet highly influences the pressure drop at 5750 rpm. At this engine speed, a pressure drop of 0.4 bar was obtained using a 60 mm trumpet. When using a 240-mm trumpet, a 0.6-bar pressure drop was obtained at high engine speed. The intake valve starts to close at 365 degrees and causes the reduction of the cylinder air intake area. At this angle, the pressure inside the air trumpet starts to rise and reaches its maximum value around the intake valve closing angle (574 degrees). The maximum pressure rise inside the trumpet is in a similar range as the maximal pressure drop.

The results of pressure fluctuation presented in Figure 8 to Figure 11 also show how pressure waves spread across the intake system. At lower trumpet lengths, higher pressure oscillations were obtained at MP2 and MP1. At MP5 and MP4, pressure oscillations were lower. When using longer trumpets, higher pressure oscillations were obtained at all measuring points. The difference in pressure oscillations influences average pressure during the air intake process, presented in Figure 12.

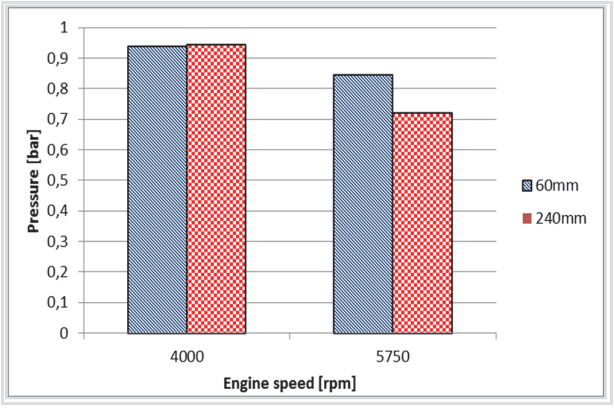


***Figure 12:*** *Average pressure in MP2 during the air intake process*

The results of average pressure inside the intake system at MP2 presented in Figure 12 indicate that at lower engine speed longer trumpet length increases air pressure during engine suction. At higher engine speeds, a shorter intake trumpet provides higher air pressure compared to a 240-mm long trumpet.

## 5 CONCLUSIONS

The influence of intake trumpet length on race car engine performance was studied numerically. The obtained results indicate that trumpet length influences the pressure fluctuation in the intake system, which further influences air mass flow per engine cycle, engine-rated power and torque.

The results of pressure fluctuations obtained at the measuring point are showing that height of the peak pressure matches the minimum value of pressure in the inlet system. According to Harrison et al. [10], this indicates that only the acoustic oscillations of air are present inside the intake system. There is no indication that shows an inertial ram effect.

At lower engine speed longer trumpets contribute to higher air mass flows and better engine performances. At higher engine speed longer trumpets tend to “choke” air flow and cause a reduction in air mass flow in comparison to shorter trumpets. This causes a reduction in engine-rated power and torque.

A longer trumpet contributed to higher air pressure during the air intake period at 4000 rpm. At 5750 rpm, the higher pressure during the intake period was obtained when using a shorter trumpet.

The optimal design of the intake system depends on desired engine specifications. If the driver wants to have the peak engine power at maximal engine power speed (5750 rpm), the optimal length of intake trumpet is 60 mm. If maximal engine power is to be obtained in the wide range of engine speeds, then 120-mm long trumpets are the optimal solution.

## 6 ACKNOWLEDGEMENTS

The presented work was supported by AVL LIST GmbH, which provided the AVL-AST software and support during the research.

## References

[1] **E.S. Dennison:** *Inertia supercharging of engine cylinders*, Transactions of the American Society of Mechanical Engineers Oil Gas and Power 55 (1933) p. p. 53-64

[2] **A. Capetti:** *Effects of intake pipe on the volumetric efficiency of an inertial combustion engine (translation)*, NACA TM 501, February 1929

[3] **C.F. Taylor, J.C. Livengood, D.H. Tsai:** *Dynamics in the inlet system of a four-stroke single cylinder engine*, Transaction on the American Society of Mechanical Engineering 77 (1955) p. p. 1133-1145

[4] **D. Jošt, A. Škerlavaj, A. Lipej:** *Improvement of Efficiency Prediction for a Kaplan Turbine,* Strojniški vestnik - Journal of Mechanical Engineering 60(2014)2, p. p. 124-134, DOI:10.5545/sv-jme. p. p. 2013.1222

[5] **J. Iljaž, L. Škerget, M. Štrakl, J. Marn:** *Optimization of SAE Formula Rear Wing*, Strojniški vestnik - Journal of Mechanical Engineering 62(2016)5, p. p. 263-272, DOI:10.5545/sv-jme.2016.3240

[6] **G. Harih, M. Tada:** *Finite element evaluation of the effect of fingertip geometry on contact pressure during flat contact*, International journal for numerical methods in biomedical engineering, ISSN 2040-7939. [Print ed.], June 2015, vol. 31, iss. 6, p. p. 1-13, doi: 10.1002/cnm.2712

[7] **G. Harih, M. Tada, B. Dolšak:** *Justification for a 2D versus 3D fingertip finite element model during static contact simulations*, Computer methods in biomechanics and biomedical engineering, ISSN 1025-5842, 2016, vol. 19, iss. 13 , p. p. 1409-1417, doi: 10.1080/10255842.2016.1146712

[8] **D.E. Winterbone, R.J. Pearson:** *Theory of Engine Manifold Design: Wave Action Methods for IC Engines,* Professional Engineering Publishing Ltd, London 2000

[9] **D. Cottyn:** *Concept design of a single cylinder F1 research engine,* MSc Thesis, Cranfield University, 2002

[10] **H.F. Harrison, A. Dunkley:** *The acoustics of racing engine intake systems,* Journal of sound and vibration 271 (2004); 959-984

[11] **Y. Xiaolong, L. Cheng, L. Jingping:** *Harmonic analysis and optimization of the intake system of a gasoline engine using GT-power,* Energy Procedia 14 (2012), p. p. 756-762

[12] **A. Sayyed:** *Air Flow Optimization through an Intake system for a Single Cylinder Formula Student (FSAE) Race Car*, International Journal of Engineering Research & Technology 6(2017), p. p. 183-188

[13] **G. Vichi, L. Romani, L. Ferrari, G. Ferrara:** *Development of an engine variable geometry intake system for a Formula SAE application,* Energy Procedia 81 (2015), p. p. 960-94

[14] **S. Pehan, B. Kegl, P. Pogorevc:** *Developing a Racing Car,* Journal of Mechanical Engineering 49(2003)12, p. p. 593-606

[15] **AVL List GmbH:** *AVL BOOST Theory*, AVL List GMBH, Graz, v2013.2 edition 11/2013

Journal of Energy Technology

JET Volume 10 (2017) p.p. 25-32
Issue 3, October 2017
Type of article 1.01
www.fe.um.si/en/jet.html

# INFLUENCE OF TAIL WATER LEVEL ON THE HYDRAULIC PERFORMANCE OF ELBOW DRAFT TUBE

# VPLIV SPODNJE VODE NA HIDRAVLIČNE KARAKTERISTIKE SESALNE CEVI

Matej Fike℟, Aleš Hribernik

**Keywords:** CFD, Elbow draft tube, Numerical analysis, Ansys CFX

## Abstract

Numerical simulations of the flow in the elbow draft tube of a Kaplan turbine were carried out in order to elucidate the effects of tail water level on draft tube performance and flow stability. The influence of the tail water level is explored considering the correct boundary condition at the inlet of the draft tube. It is found that the increasing tail water level affects the inlet boundary condition of the draft tube, the flow rate through the turbine, and draft tube. Thus, head recovery, efficiency and the possibility of cavitation phenomena decreases. However, the head loss increases, and the flow rate through the turbine and draft tube decreases.

## Povzetek

Izvedene so bile numerične simulacije toka v kolenasti sesalni cevi kaplanove turbine z namenom preučitve vpliva spodnjega nivoja gladine vode na brezdimenzionalne karakteristike in na stabilnost toka v sesalni cevi. Vpliv nivoja spodnje vode je raziskan z upoštevanjem pravilnih robnih pogojev na vstopu. Ugotovljeno je bilo, da naraščanje spodnjega nivo vode vpliva na pretok skozi turbino in posledično na vstopni robni pogoj sesalne cevi. Posledično se izkoristek in verjetnost nastanka kavitacije zmanjša. Na drugi strani se hidravlične izgube povečajo, pretok skozi turbino in sesalno cev pa se zmanjša.

℟ Corresponding author: Matej Fike, Faculty of Energy Technology, Hočevarjev trg 1, SI-8270 Krško, Tel.: +386 7 6202 228, E-mail address: matej.fike@um.si

# 1 INTRODUCTION

Hydropower plays an important role in the energy sector and helps to meet increasing demand for energy. The hydraulic turbines convert hydro energy into electric energy and, therefore, the increase in efficiency of the turbine is an important task. Each component of turbine has some specific function, and hence the design of every component of the turbine is equally important. However, out of all components, draft tube converts kinetic energy coming out of runner into useful pressure energy that would otherwise be wasted. Therefore, the design of the draft tube is important and contributes to improving the efficiency and overall performance of the turbine.

The main aim of this research was to examine flow conditions within the draft tube of a hydropower plant at different tail water levels using 3D CFD simulation to inspect for possible irregularities within the flow.

Numerical flow simulation has been carried out for steady viscous turbulent flow in a Kaplan turbine assembly consisting of a semi-spiral casing with stay and guide vanes, a 4-blade runner and an elbow draft tube using Ansys CFX commercial CFD code. The $k$-$\varepsilon$ turbulence model has been used. The head loss, head recovery, and efficiency characteristics of the draft tube have been predicted at low, normal and high-water conditions using simulation results (at three different tail water levels). In addition, velocity streamlines and contours of velocities and pressure at selected planes within the draft tube have been obtained.

# 2 NUMERICAL MODEL

Commercial CFD software Ansys CFX 16.2 was used for this study. Simulations of two-phase flows can be achieved by assuming the vapor/liquid mixture as a multi-phase single fluid, with variable densities. No slip exists between the two phases in this mixture model. We performed analyses with the $k$-$\varepsilon$ turbulence model with scalable wall functions.

## 2.1 Geometry

Three-dimensional geometry of the draft tube was modelled in SolidWorks. The numerical model consists of two main parts: draft tube and draft tube prolongation. The inlet cross-section is a circle with a diameter of 1.6 m. The outlet cross-section is a rectangle 5 m in width and 1 m in height. The length of the draft tube is 8.2 m. Draft tube prolongation (Figure 1) with the free surface between the air and water stream was added to properly simulate the outflow conditions and to avoid any influence of the outflow boundary conditions on the draft tube flow.

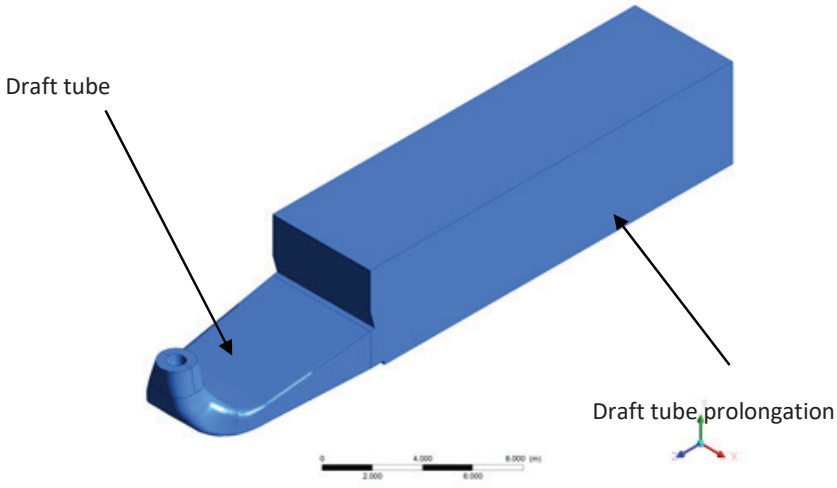


***Figure 1:*** *Draft tube model with draft tube prolongation*

## 2.2 Mesh creation

Structured computational meshes were used in all parts and were designed with ICEM CFD 16.0 software. Numbers of elements used are specified in Table 1.

***Table 1:*** *Mesh data*

| Domain | Nodes | Elements |
|---|---|---|
| Draft tube | 382,328 | 387,971 |
| Draft tube prolongation | 630,350 | 605,395 |
| All Domains | 1,012,678 | 993,366 |

Figure 2 shows the structural mesh of a draft tube and a draft tube with prolongation. The resolution of the mesh is greater in regions where greater computational accuracy is needed, such as close to the inlet and close to the walls.

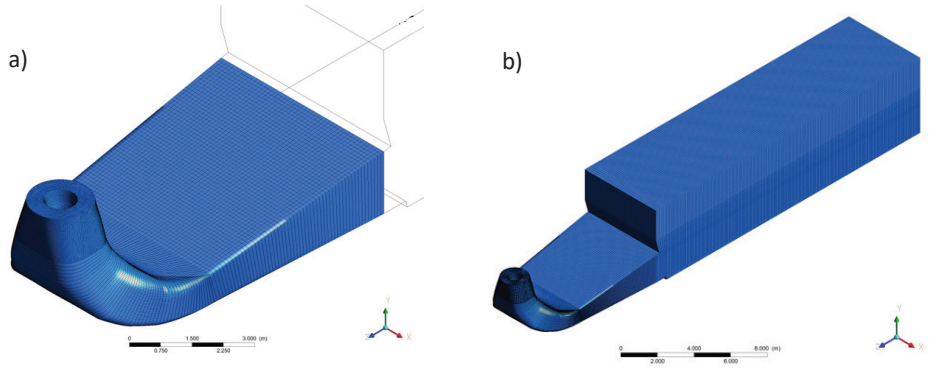


***Figure 2:*** *Numerical mesh a) draft tube and b) draft tube with prolongation*

## 2.3 Boundary conditions and convergence criteria

Correct inflow boundary conditions are necessary in order to correctly simulate the flow conditions within the draft tube. These may be prescribed by experimental data or by the application of a turbine model for their prediction. The turbine model was used in our case. A simplified turbine model was used for the optimal set of guide vane and runner blade angles. Only the guide vane passage and rotor blade passage flows were simulated.

The guide vane passage flow was simulated within the static frame while rotor passage flow was within the rotational frame of reference. The interface boundary condition was applied to connect both frames. Using the periodic boundary condition on both sides of the simulated flow passages, it was possible to simulate only one pair of passages and not the whole turbine.

At the inlet and at the exit of the domain, static pressure was prescribed. This enabled predicting the flow rate and velocity components at the outlet of the rotor for different available heads.

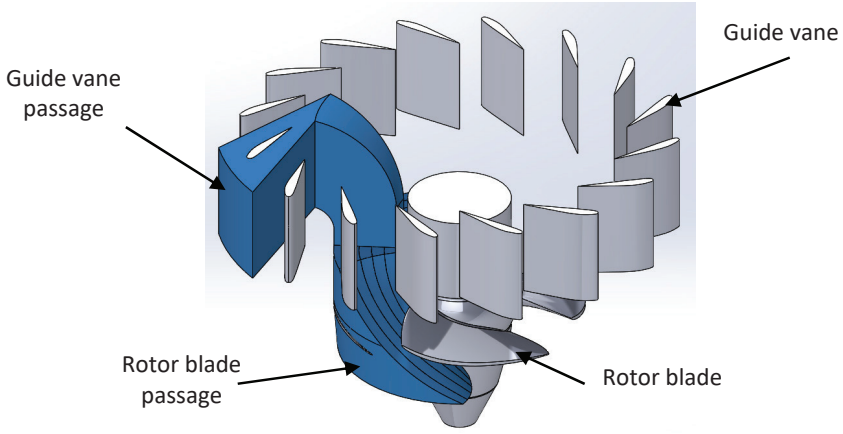


***Figure 3:*** *Inlet boundary conditions*

Three different inlet boundary conditions were prescribed in order to perform simulations of the flow within the draft tube for low, normal and high-water conditions.

***Table 2:*** *Inlet boundary conditions*

| Water conditions | Low | Normal | High |
|---|---|---|---|
| Tail Water level | H-1m | H | H+1m |
| Volume Flow Rate | 13.2 $m^3/s$ | 13.6 $m^3/s$ | 14.1 $m^3/s$ |
| Head | 5.7 m | 6.7 m | 7.7 m |

Low water condition Normal water condition High water condition

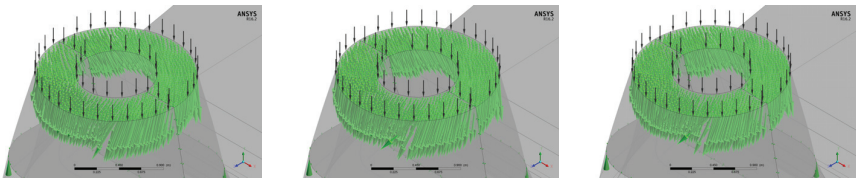

***Figure 4:*** *Inlet boundary conditions*

Although the flow within the draft tube is almost always unsteady, steady-state simulations were used in order to substitute time-consuming and expensive unsteady simulations. Previous research determined that steady-state simulations assure reliable results.
Draft tube prolongation with the free surface between the air and water stream was added to properly simulate the outflow conditions and to avoid any influence of the outflow boundary conditions on draft tube flow.
The relative hydraulic pressure at the outlet of the draft tube prolongation with the following equation was prescribed (Figure 5).

$$p = g \cdot \rho \cdot VFW \cdot (H - y) \tag{2.1}$$

where:

VFW - volume fraction of water
H - tail water height

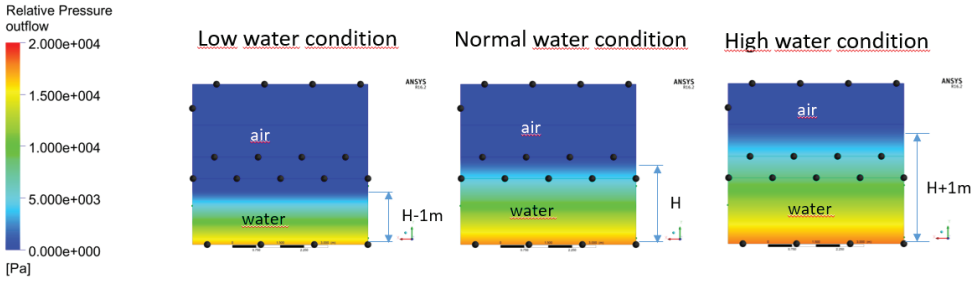


***Figure 5:*** *Outlet boundary conditions*

To satisfy the convergence criteria, all the RMS (root mean square) residuals from solving equations must be under $1 \cdot 10^{-5}$. We also set the number of maximum iterations to 500 and used automatic timescale control.

# 3 RESULTS

## 3. 1 Characteristic parameters

The computed results of the flow in the draft tube at different tail water levels were compared with the following non-dimensional hydrodynamic parameters.

Head loss in draft tube

$$H_{LD} = \frac{p_{tin} - p_{tout}}{\rho g} \tag{3.1}$$

Head recovery in draft tube

$$H_{RD} = \frac{v_{in}^2 - v_{out}^2}{2g} - H_{LD} \tag{3.2}$$

Efficiency of draft tube

$$\eta_D = \frac{2gH_{RD}}{v_{in}^2} \times 100 \tag{3.3}$$

where:

$H_{LD}$ *=head loss in draft tube (m)*

$p_{tin}$ *=total pressure at draft tube inlet (Pa)*

$p_{tout}$ *=total pressure at draft tube outlet (Pa)*

$\rho$ *=specific mass of fluid (kg/ ³)*

$g$ *=acceleration due to gravity (m/s ²)*

$v_{in}$ *=velocity at draft tube inlet (m/s)*

$v_{out}$ *=velocity at draft tube outlet (m/s)*

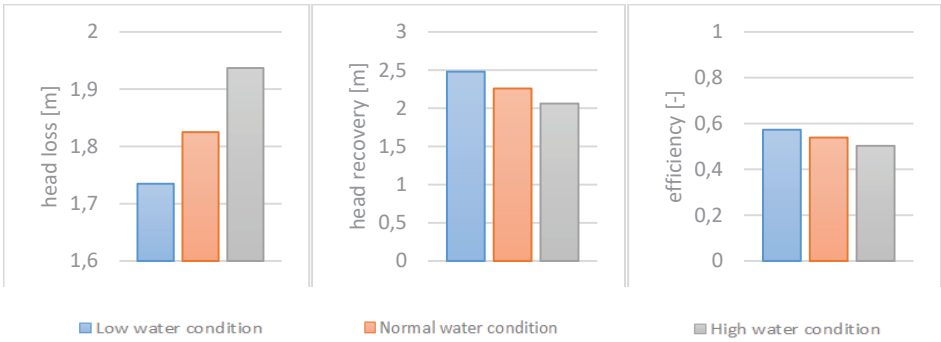


***Figure 6:*** *Head loss, head recovery and efficiency for different tail water levels*

Diagrams of head loss, head recovery and efficiency are presented in Figure 6. It can be observed that with tail water increases, head loss parameter increases, while head recovery and efficiency decrease.

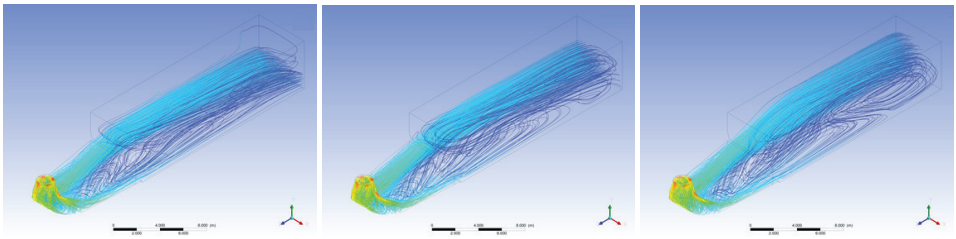

Low water condition | Normal water condition | High water condition

***Figure 7:*** *Velocity streamlines*

Figure 7 shows velocity streamlines within the draft tube. In the draft tube inflow section, the flow is concentrated near the walls due to small tangential velocity component induced by the runner blade passage. A wake is, therefore, formed in the middle of the stream and it is extended far into the draft tube prolongation. The velocity profile is very asymmetric.

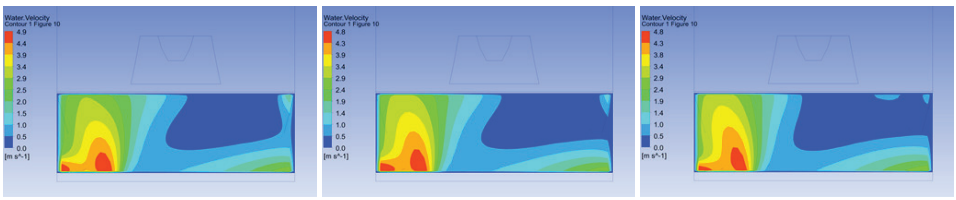

Low water condition | Normal water condition | High water condition

***Figure 8:*** *Velocity contours*

Velocity contours at the outlet of the draft tube are presented in Figure 8 for three different tail water levels. The high-velocity stream can be seen at the bottom left side of the draft tube with its peak near the bottom in all three cases. All three velocity plots are similar. The difference is in the magnitude of the velocity, which depends on the volume flow rate through the draft tube.

## 4 CONCLUSIONS

In this paper, numerical simulations of the flow in the draft tube of a Kaplan turbine were carried out to elucidate the effects of tail water level on draft tube performance and flow stability. The tail water level significantly affects the performance of the turbine, when the guide vane and rotor blade angle settings remain unchanged. The influences of the increasing tail water level are as follows:

- the flow rate through turbine and draft tube decreases, and affects the inlet boundary condition of the draft tube
- the head loss increases
- head recovery decreases
- efficiency decreases
- the possibility of cavitation phenomena decreases

## References

[1] **H. Dou, L. Niu, and S. Cao**: *Effects of tangential velocity distribution on flow stability in a draft tube*, Journal of Thermal Science, vol. 23, no. 5, pp. 446–453, 2014

[2] **H. Ying, C. Heming, W. Quanlong, and Y. Zhikun**: *Computer simulation of turbulent flow through a hydraulic turbine draft tube*, Wuhan University Journal of Natural Sciences, vol. 11, no. 3, pp. 649–652, 2006

[3] **Z. G. Zuo, S. H. Liu, D. M. Liu, and D. Q. Qin:** *Numerical predictions and stability analysis of cavitating draft tube vortices at high head in a model Francis turbine*, Science China Technological Sciences, vol. 57, no. 11, pp. 2106–2114, 2014

[4] **L. Motycak, A. Skotak, and J. Obrovsky:** *Analysis of the Kaplan turbine draft tube effect*, Earth and Environmental Science, vol. 12, 2010

Journal of Energy Technology

JET Volume 10 (2017) p.p. 33-45
Issue 3, October 2017
Type of article 1.04
www.fe.um.si/en/jet.html

# ANALYSIS OF OUTDOOR LED LIGHTING'S DIMMING INFLUENCE ON THE PERFORMANCE OF LED DRIVERS

# ANALIZA VPLIVA ZATEMNJEVANJA ZUNANJE LED RASVETLJAVE NA UČINKOVITOST LED KRMILNIKOV

Jurica Perko✉, Denis Pelin[1], Danijel Topic[2]

**Keywords:** Outdoor LED lighting, LED driver, constant current driver, efficiency, THDI, dimmer control, pulsation, output voltage ripple

## Abstract

With the development of new technologies, LEDs (light-emitting diodes) take a significant position in lighting due to their long-life spans and high luminous efficacy, which result in energy and maintenance cost savings. These efficient and innovative light sources require adequate ballast or electronic control gear, also known as LED drivers, for their operation. An LED driver provides appropriate voltage level and current for the operation of LEDs. It converts and rectifies higher voltages of alternating current to lower voltages of direct current and regulates the current flowing through LEDs at a nominal level. There are many advantages and disadvantages to using LEDs, primarily caused by LED circuits and LED drivers. The dimming influence of outdoor LED lighting on the LED driver performance is analysed in this paper, specifically the testing of an LED lighting driver by changing the load level.

✉ Corresponding author: Jurica Perko MEng, Regional Energy Agency North, M. Krleze 81, 48000 Koprivnica, Croatia Tel.: +385 95 904 1543, E-mail address: jurica.perko@rea-sjever.hr

[1] Faculty of Electrical Engineering, Computer Science and Information Technology Osijek, Department of Electromechanical Engineering, Kneza Trpimira 2B, 31000 Osijek, Croatia

[2] Faculty of Electrical Engineering, Computer Science and Information Technology Osijek, Department of Power Engineering, Kneza Trpimira 2B, 31000 Osijek, Croatia

Results of LED driver efficiency calculated from measured input and output power, output voltage ripple measurements, and total harmonic distortion analysis are shown. Based on the measurement results, significant recommendations and concluding remarks are given.

## Povzetek

Z razvojem novih tehnologij je LED tehnologija (light-emitting diodes, svetleče diode) zavzela pomemben delež v razsvetljavi, predvsem zaradi dolge življenjske dobe in visoko učinkovite svetilnosti, kar omogoča prihranke pri stroških za energijo in vzdrževanje. Tako učinkoviti in inovativni viri svetlobe za svoje delovanje zahtevajo ustrezen balast ali sklope za elektronsko krmiljenje oziroma LED krmilnike. LED krmilnik omogoča ustrezno napetost in tok za delovanje LED-a, tako da pretvarja in gladi izmenični tok z visoko napetostjo v enosmerni tok z nizko napetostjo in vzdržuje nominalno raven toka skozi LED žarnico. Obstaja veliko razlogov za ali proti uporabi LED žarnico, kar je odvisno od LED vezij in LED krmilnikov. V članku je analiziran vpliv uporabe zatemnitve zunanje LED razsvetljave na učinkovitost LED krmilnikov. Članek predvsem opisuje preizkušanje krmilnika LED razsvetljave s spreminjanjem bremena in prikazuje rezultate učinkovitosti LED krmilnika, ki so izračunani na podlagi meritev vhodne in izhodne moči, meritev utripanja in celovite analize harmoničnega popačenja. Na podlagi rezultatov meritev so podane zaključne opombe in pomembna priporočila.

# 1 INTRODUCTION

As the next generation of lighting sources, LED street lighting has numerous advantages, such as high efficiency, power saving, cold start, longer lifetime, and improved brightness. LED lighting is practicable and reduces electricity consumption, resulting in cost reductions, *[1]*. It is distinguished by a positive impact on the environment and long life that results in maintenance cost reductions. LEDs require a low voltage DC supply, which necessitates AC/DC conversion if they are powered by an AC supply. LED drivers should meet the requirements according to the standards IEC 62384, ANSI C82-SSL 1-200X, and ANSI C82.77. The author of *[2]* recommends more stringent requirements as shown below:

1. power factor > 0.9
2. power efficiency > 85%
3. compliance with energy regulations
4. constant current output
5. high reliability
6. protection (surge, overvoltage, overload, short circuit, etc.)
7. low ripple
8. operation temperature -40 °C – +70 °C.

These requirements will be used in further analysis due to the fostering of energy efficiency. The requirements listed above indicate that an LED lighting driver includes the following modules: diode bridge rectifier, power factor correction (PFC), electromagnetic interference filter (EMI),

pulse-width modulation (PWM), overvoltage protection (OVP), overload protection (OLP) and overcurrent protection (OCP) as shown in Figure 1 and described in Table 1. As a part of the diode bridge rectifier, an LED driver also includes a negative temperature coefficient thermistor (NTC), Table 1.

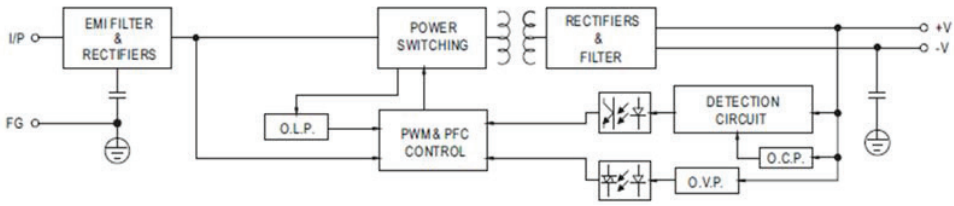


***Figure 1:*** *Block diagram of the LED driver, [3]*

***Table 1:*** *Basic information of LED driver modules*

| | |
|---|---|
| Rectifier | Full-wave bridge rectifier of a single-phase supply converts the entire waveform to one of constant polarity at its output (positive or negative). It is also known as a Graetz bridge rectifier, a full-wave rectifier using four diodes. |
| PFC | Power factor correction is a feature that reduces the amount of reactive power generated from a lamp. It changes the waveform of current drown by a load to improve the power factor. |
| EMI | Electromagnetic interference is a passive electronic device that is used to damp a disturbance generated by an external source that affects an electrical circuit. |
| NTC | A NTC thermistor limits inrush current. When the circuit is closed, resistance decreases as the temperature rises, in other words, by the time, current heated thermistor, and its resistance changes to a lower value, allowing uninterrupted flow of current. |
| PWM | Pulse-width modulation is a modulation technique used for LED lighting intensity control. |
| OVP | Overvoltage protection is used to detect and quickly reduce the overvoltage condition to prevent damage. |
| OLP | Overload protection is a protection against a running overcurrent that would cause overheating of the LED driver. |
| OCP | Overcurrent protection is protection against excessive currents or current beyond the acceptable current rating of the LED driver. |

There are many different types and variations of LED drivers, but they are mainly divided into two basic types:

1. constant current (CC) drivers
2. constant voltage (CV) drivers.

LEDs are driven by constant current (typically 350 mA, 700 mA or 1A) drivers that fix the current of the system and vary the voltage depending on the load of the LED or constant voltage (typically 10 V, 12 V or 24 V) drivers that require a fixed voltage, according to which the LED loads are added in parallel across the output of the driver until maximum output currents are reached. There are also LED manageable drivers that make LEDs more efficient. A manageable driver is a constant current driver that provides exact current on an LED module lower than nominal current. By applying that, it is possible to change the light intensity level.

# 2 MATERIALS AND METHOD

## 2.1 Equipment and measuring instruments

The LED lamp used for testing is a low-energy alternative for a 75 W high-pressure sodium lamp. It is intended for outdoor lighting. The lamp is closed in accordance with the IP66 degree of protection, which proves its resistance to dust and water splashes. It gives natural white light, which enables much better visibility and better contrast in comparison with high-pressure sodium lamps. The main characteristics of the tested lamp and LED driver are given in Table 2 and Table 3.

***Table 2:*** *Main characteristics of LED lamp*

| Parameter | Unit | Value |
|---|---|---|
| Input voltage | V | 230 |
| Frequency | Hz | 50–60 |
| Nominal power | W | 40 |
| Correlated colour temperature | K | 4,000 |
| Color rendering index | - | 70–80 |
| Luminous flux | lm | 3,000 |

***Table 3:*** *Main characteristics of LED driver*

| Parameter | Unit | Value |
|---|---|---|
| Input voltage | VAC | 100–240 |
| Frequency | Hz | 50–60 |
| Input current | A | 0.8 |
| Maximum input power | W | 80 |
| Inrush current | $A^2s$ | 0.35 |
| Output voltage | VDC | 25–50 |
| Output current | mA | 1,050 |
| Maximum output power | W | 52 |

The instruments used for measuring were a digital four-channel storage oscilloscope (100 MHz with 1 GS/s sample rate on all channels), a high-precision power analyser (1 MHz / 341 kHz sample rate), which is used for measuring input current, voltage, active and reactive power, power factor, THDI and output current, voltage and active power of LED driver.

To display current waveforms, current probes (AC/DC – 100 kHz, 50 mA to 100 A peak) were used.

## 2.2 Methodology of measurements

The main objective of these measurements is to examine the efficiency of the LED driver and to show the dimming influence on its performance. Using the above-mentioned measuring instruments and electronic test instrument the following measuring units are recorded, and the change of characteristic waveforms over time are observed:

- measured values
    - input and output voltage [V]
    - input and output current [mA]
    - input and output power [W]
    - power factor
    - reactive power [VAr]
    - output voltage ripple [V]
    - THDI [%]

- observed change of a characteristic waveform
    - input voltage
    - input current
    - output voltage.

Input and output terminals of observed LED lighting driver were connected to a multi-channel power analyser that can measure both DC and AC components.

To test an LED lighting driver for different power levels, one of the possible dimming implementations (DC input, external resistor or reverse external resistor) must be used. The dimmer control may be operated via a dimmer or from an input signal of 0–10 VDC. When performing these measurements, an external resistor is used for the purpose of dimming, Figure 2. It is also known as a potentiometer, which is a three-terminal resistor with a rotating contact that forms an adjustable voltage divider.

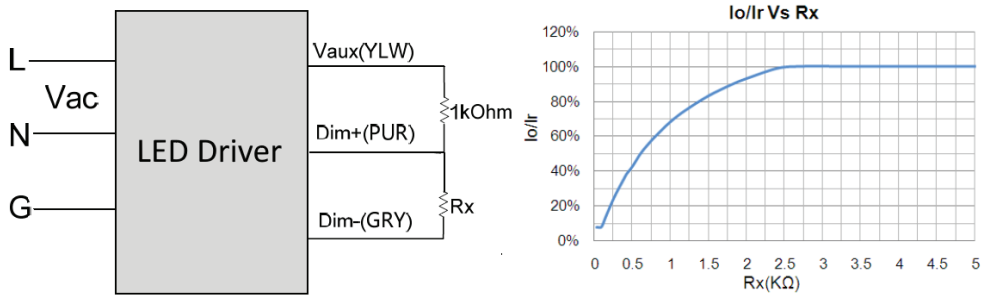


***Figure 2:*** *Dimmer control – external resistor [4]*

The measurements were conducted between 20% and 100% of the nominal load at increments of 5%. Figure 2 shows that the lower limit of dimming is 10% of the nominal load; we chose to conduct measurements from 20% of the nominal load.

# 3 RESULTS AND DISCUSSION

## 3.1 Efficiency analysis

Efficiency analysis includes measurements of LED drivers input and output voltage, current and power starting from 20% of the nominal load to full power operation at increments of 5%. The efficiency of LED driver has been calculated by the following equation:

$$\eta = \frac{P_{out}}{P_{in}} \cdot 100\% \tag{3.1}$$

The results of measurements are presented in continuation, Table 4 and Figure 3. It was observed that efficiency decreases with decreasing load level. For loads lower than 40% of nominal load,

efficiency rapidly decreases to almost 70%. According to *[2]*, it is acceptable to dim LED lighting up to 35% of nominal load because an LED driver should meet power efficiency higher than 85%.

***Table 4:*** *Results of efficiency measurements*

| Load [%] | Input voltage [V] | Input current [mA] | Input power [W] | Output voltage [V] | Output current [A] | Output power [W] | Efficiency [%] |
|---|---|---|---|---|---|---|---|
| 20 | 233.11 | 73.41 | 9.96 | 34.43 | 0.21 | 7.27 | 73.03 |
| 25 | 232.46 | 77.79 | 11.35 | 34.78 | 0.25 | 8.72 | 76.84 |
| 30 | 231.12 | 85.10 | 13.46 | 35.26 | 0.31 | 10.97 | 81.52 |
| 35 | 230.96 | 92.63 | 15.73 | 35.70 | 0.37 | 13.31 | 84.60 |
| 40 | 230.16 | 100.97 | 18.32 | 36.15 | 0.44 | 15.95 | 87.08 |
| 45 | 230.82 | 110.21 | 20.55 | 36.49 | 0.50 | 18.19 | 88.52 |
| 50 | 231.84 | 118.44 | 22.34 | 36.75 | 0.55 | 19.97 | 89.39 |
| 55 | 232.92 | 127.89 | 24.55 | 37.06 | 0.60 | 22.17 | 90.31 |
| 60 | 230.31 | 137.41 | 27.18 | 37.41 | 0.67 | 24.82 | 91.32 |
| 65 | 232.18 | 137.02 | 29.19 | 37.66 | 0.72 | 26.82 | 91.88 |
| 70 | 232.27 | 140.94 | 31.52 | 37.94 | 0.77 | 29.11 | 92.35 |
| 75 | 233.25 | 149.12 | 33.66 | 38.19 | 0.82 | 31.19 | 92.66 |
| 80 | 231.51 | 162.31 | 36.55 | 38.51 | 0.89 | 34.05 | 93.16 |
| 85 | 227.71 | 171.96 | 38.25 | 38.71 | 0.93 | 35.72 | 93.39 |
| 90 | 226.31 | 183.33 | 40.67 | 38.99 | 0.99 | 38.08 | 93.63 |
| 95 | 229.28 | 188.91 | 42.48 | 39.24 | 1.02 | 39.79 | 93.67 |
| 100 | 230.45 | 199.04 | 45.04 | 39.64 | 1.08 | 42.25 | 93.81 |
| Average efficiency [%] | | | | | | | 88.66 |

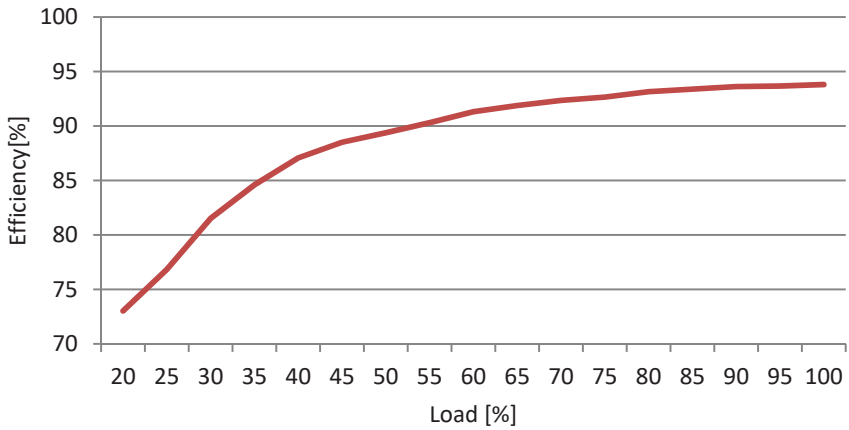


***Figure 3:*** *Dependence of efficiency on load level*

Load level dependence on power factor and reactive power is shown as follows, Table 5, Figure 4 and Figure 5. The power factor has two stages of rapid decreasing in dependence on load level change. First one is between 70% and 55% of nominal load, and the second one is in the range from 40% to 20%. Reactive power rapidly decreases at dimming stages lower than 70% of nominal load, but most of the national utility companies still do not charge reactive power in the tariff model for public lighting.

***Table 5:*** *Results of power factor measurements*

| Load [%] | Power factor | Reactive power [VAr] |
|---|---|---|
| 20 | 0.5823 | 13.91 |
| 25 | 0.6277 | 14.08 |
| 30 | 0.6842 | 14.34 |
| 35 | 0.7353 | 14.50 |
| 40 | 0.7883 | 14.30 |
| 45 | 0.8080 | 14.99 |
| 50 | 0.8136 | 15.97 |
| 55 | 0.8241 | 16.72 |
| 60 | 0.8587 | 16.22 |
| 65 | 0.9174 | 12.66 |
| 70 | 0.9628 | 8.85 |
| 75 | 0.9677 | 8.77 |
| 80 | 0.9727 | 8.72 |
| 85 | 0.9769 | 8.37 |
| 90 | 0.9803 | 8.19 |
| 95 | 0.9807 | 8.46 |
| 100 | 0.9820 | 8.66 |

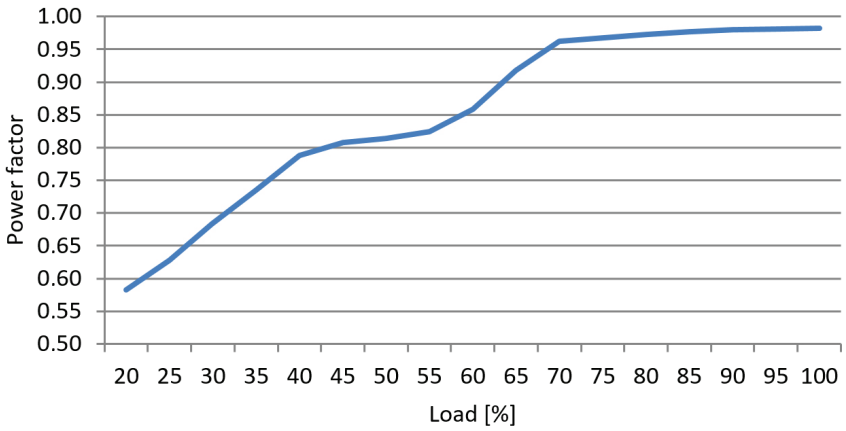


***Figure 4:*** *Dependence of power factor on load level*

To foster energy efficiency, it is acceptable to dim LED lighting up to 65% to meet the LED driver requirement for a power factor higher than 0.9, *[2]*. In any case, the LED driver meets the Standard ANSI C82.77, which requires a minimum power factor of 0.5. It could be noted that reactive power is approximately constant while dimming in a range from 70% to 100% of the nominal load (Figure 5). An LED lamp, as a typical electronic end-user device, has a capacitive load. It affects the network with reduced power delivery, which means that reactance increases losses and possibly limits the available power.

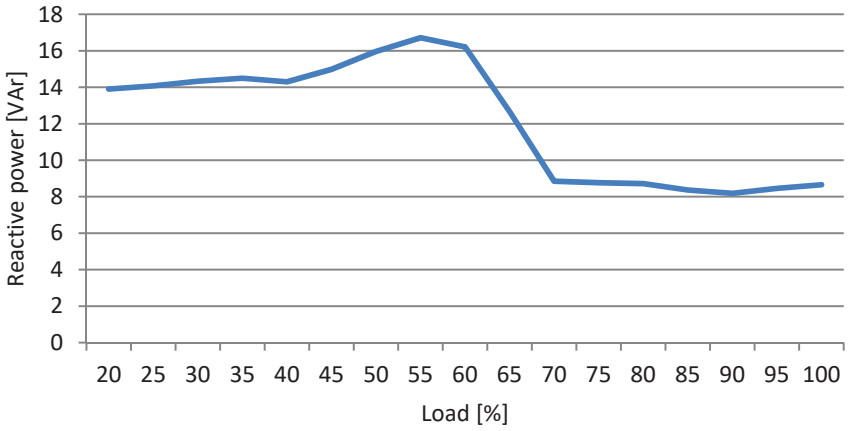


***Figure 5:*** *Dependence of reactive power on load level*

## 3.2 Output voltage ripple and harmonic distortion analysis

It is well known that a full-wave bridge rectifier converts the whole of the input waveform to a constant polarity at its output, either positive or negative. It converts both polarities of the input waveform to pulsating DC, *[5]*. Output voltage ripple often could cause light output fluctuations, especially at the full power operation mode of an LED lighting lamp that has the greatest spread between peaks at this stage. The output voltage ripple of the tested LED lighting lamp is shown in Table 6, and the pulsating DC voltage component in comparison with the input current waveform is shown in Figure 6.

***Table 6:*** *Results of output voltage ripple*

| Load [%] | Peak $U_p$+[V] | Peak $U_p$-[V] | Output voltage ripple [V] |
|---|---|---|---|
| 20 | 34.70 | 34.07 | 0.63 |
| 25 | 35.09 | 34.37 | 0.72 |
| 30 | 35.63 | 34.75 | 0.88 |
| 35 | 36.15 | 35.08 | 1.07 |
| 40 | 36.66 | 35.45 | 1.21 |
| 45 | 37.05 | 35.72 | 1.33 |
| 50 | 37.34 | 35.91 | 1.43 |
| 55 | 37.69 | 36.17 | 1.52 |
| 60 | 38.12 | 36.45 | 1.67 |
| 65 | 38.50 | 36.64 | 1.86 |
| 70 | 38.92 | 36.84 | 2.08 |
| 75 | 39.24 | 37.01 | 2.23 |
| 80 | 39.67 | 37.23 | 2.44 |
| 85 | 39.92 | 37.37 | 2.55 |
| 90 | 40.27 | 37.56 | 2.71 |
| 95 | 40.58 | 37.74 | 2.84 |
| 100 | 40.93 | 37.96 | 2.97 |

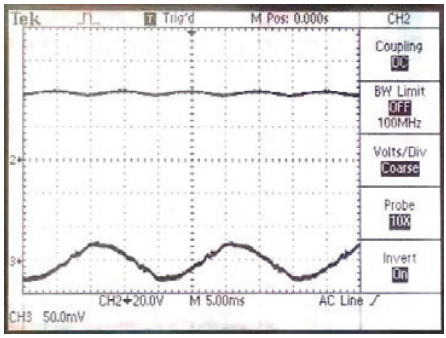


***Figure 6:*** *Pulsation of output voltage (CH2) and input current (CH3) for 100% of nominal load*

The output voltage ripple at a load level of 100% is maximum, 3 V, which means that the light output fluctuation at this load level is the greatest.

The pulsating AC component of output voltage in comparison with the input current waveform for load level of 20%, 40%, 70%, and 100% of the nominal load is shown in continuation, Figure 7.

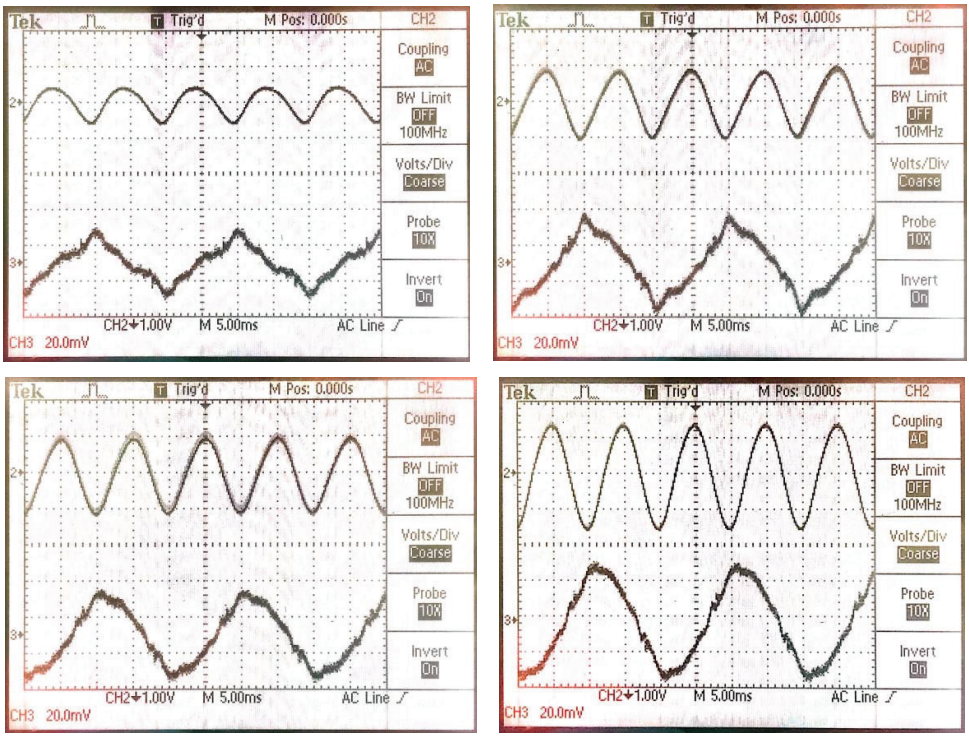


***Figure 7:*** *Pulsation at a) 20% b) 40% c) 70% and d) 100% of nominal load – AC voltage and current component*

An LED lighting lamp, as a digital device, brings interferences into the distribution network as a total harmonic distortion of current (THDI). Table 7 shows the share of each harmonic and total harmonic distortion for each load level (Figure 8).

The THDI measurements presented in Table 7 include only the first 15 odd harmonics that are calculated with the following equation:

$$THDI = \frac{100}{I_1} \cdot \sqrt{\sum_{n=2}^{15} \left( \frac{I_{n,rel}}{100} \cdot I_1 \right)^2} \tag{3.2}$$

***Table 7:*** *Harmonic analysis*

| Load [%] | Harmonic [%] | | | | | | | | THDI [%] |
|---|---|---|---|---|---|---|---|---|---|
| | 1st | 3rd | 5th | 7th | 9th | 11th | 13th | 15th | |
| 20 | 100.00 | 28.00 | 14.00 | 8.40 | 1.00 | 2.50 | 1.90 | 3.10 | 32.73 |
| 25 | 100.00 | 28.10 | 14.00 | 7.90 | 1.00 | 2.70 | 1.70 | 2.90 | 32.67 |
| 30 | 100.00 | 27.00 | 11.90 | 5.40 | 2.80 | 3.70 | 1.60 | 4.90 | 30.79 |
| 35 | 100.00 | 22.60 | 12.50 | 6.10 | 1.10 | 1.80 | 0.70 | 3.10 | 26.81 |
| 40 | 100.00 | 20.80 | 13.00 | 5.60 | 1.30 | 1.30 | 0.40 | 2.80 | 25.38 |
| 45 | 100.00 | 21.20 | 14.60 | 5.50 | 2.10 | 0.30 | 1.20 | 2.80 | 26.58 |
| 50 | 100.00 | 22.00 | 15.50 | 5.90 | 2.80 | 0.20 | 1.20 | 2.30 | 27.81 |
| 55 | 100.00 | 22.80 | 17.10 | 7.00 | 3.70 | 0.50 | 0.60 | 1.80 | 29.64 |
| 60 | 100.00 | 21.50 | 16.00 | 7.10 | 4.10 | 0.40 | 0.20 | 1.60 | 28.08 |
| 65 | 100.00 | 14.00 | 10.80 | 6.30 | 3.60 | 0.40 | 0.30 | 1.80 | 19.20 |
| 70 | 100.00 | 6.20 | 4.30 | 3.90 | 0.60 | 1.70 | 0.70 | 1.60 | 8.86 |
| 75 | 100.00 | 5.50 | 3.30 | 3.60 | 0.80 | 1.50 | 0.60 | 1.50 | 7.72 |
| 80 | 100.00 | 4.90 | 3.80 | 4.40 | 1.30 | 1.20 | 0.70 | 1.40 | 7.96 |
| 85 | 100.00 | 4.70 | 3.30 | 3.50 | 1.00 | 1.50 | 0.60 | 1.40 | 7.13 |
| 90 | 100.00 | 4.50 | 3.30 | 3.40 | 1.20 | 1.40 | 0.60 | 1.10 | 6.90 |
| 95 | 100.00 | 4.50 | 3.10 | 3.80 | 1.60 | 1.30 | 0.80 | 1.20 | 7.12 |
| 100 | 100.00 | 4.40 | 3.30 | 4.20 | 1.80 | 1.20 | 0.90 | 1.00 | 7.37 |

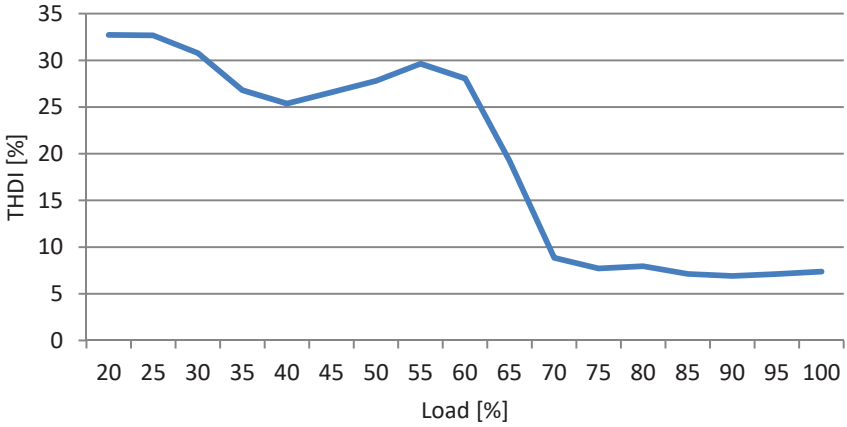


***Figure 8:*** *Dependence of THDI on load level*

It was observed that THDI is approximately constant in the range from 70% to 100% of nominal load and does not exceed 10%. Input current waveform in comparison with input voltage waveform is shown in continuation, Figure 9.

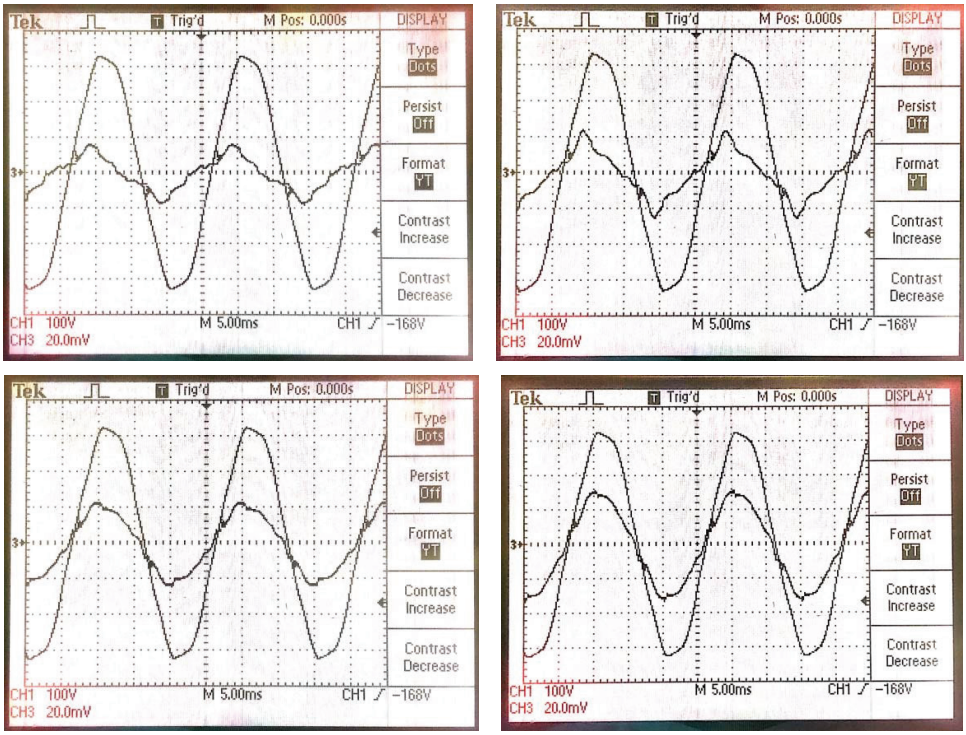


***Figure 9:*** *Input current and voltage waveform for a) 20%, b) 40%, c) 70%, and d) 100% of nominal load*

Figure 9 shows the first harmonic current shift in comparison with the input voltage at lower loads, which could be explained by the low value of the power factor, Figure 4. It could be noted that current leads voltage which implies to capacitive load. Lower loads also result in worst harmonic content, Figure 8.

## 4 CONCLUDING REMARKS

Public lighting is supplied from public lighting cabinets, mostly located with a distributive transformer station. Except for the metering point, public lighting cabinets consist of protective equipment and devices for the regulation of light intensity. Because LED lighting is supplied by 230 V AC and 50 Hz, like conventional street lighting, there is no need for any additional infrastructure interventions, *[6]*. This paper deals with analysis of outdoor LED lighting dimming influence on the LED drivers' efficiency and the influence of dimming on performance. LED drivers were previously researched in *[7]*, *[8]*, and *[9]*.

As expected, the LED driver complies with the requirements of the applicable standards but with the aim of improving energy efficiency; the LED driver is analysed according to the requirements listed in [2]. The results of efficiency analysis showed that LED efficiency decreases with decreasing light intensity, i.e. by dimming. There is also similar dimming impact on power factor change.

As mentioned above, the LED driver comprises a full-wave bridge rectifier, by which LEDs are modulated at twice the AC frequency. Luminous intensity is proportional to the current LED flickers at this rate. LEDs have a certain time to completely stop producing photons during the off part of the waveform, which is a negative point in comparison to other conventional light sources. Output voltage ripple analysis showed that light output fluctuations, (flickering) are more expressed in LEDs in full operation mode.

Harmonic analysis reveals that THDI is approximately constant and does not exceed 10% in the range from full power operation to operation at 70% of the nominal load. It can be observed that a huge THDI step exists at operations lower than 70%.

Generally, testing of the LED module and LED driver supported the recommendation for LED dimming possibilities in terms of energy efficiency and LED driver performance. It is recommended for LED lighting to operate at a minimum of 70% of nominal load to meet LED driver requirements according to *[2]*. It is also important to note that although it is possible to change the load level from 100% to 10% of nominal load (i.e. to dim LED lighting), the LED driver producer does not provide measurement results for cases from 10% to 50% in the data sheets, *[4]*. Obviously, the reason lies in poor values. Finally, the authors provide a conclusion: higher load leads to better energy efficiency indicators but does not have an output voltage ripple.

## References

[1] **J. Perko, D. Topic, D. Sljivac**: *Exploitation of public lighting infrastructural possibilities,* Proceedings of 2016 International Conference on Smart System and Technologies, 2016, Osijek, Croatia

[2] **Farnell element14**: *LED Street Lighting,* Available: http://uk.farnell.com/led-street-lighting-applications, (9 March 2017)

[3] **Mean Well**: *60W Single Output LED Power Supply*, Available: http://www.meanwell.com/webapp/product/search.aspx?prod=CLG-60, (10 March 2017)

[4] **Inventronics**: *52W Constant Current IP67 Driver,* Available: http://www.inventronics-co.com/upload/EUC-052SxxxDV(SV)_20160418102235812 11.PDF, (13 March 2017)

[5] **B.W. Williams**: *Power electronics: devices, drivers and applications,* Basingstoke: Macmillan, 1992

[6] **Digi-Key electronics**: *Characterizing and Minimizing LED Flicker in Lighting Applications,* Available: https://www.digikey.com/en/articles/techzone/2012/jul/characterizing-and-minimizing-led-flicker-in-lighting-applications, (21 March 2017)

[7] **L. Yu, J. Yang**: *The topologies of white LED lamps' power drivers*, Proceedings of 2009 3rd International Conference on Power Electronic Systems and Applications, 2009, Hong Kong, Hong Kong

[8] **C. Moo, Y. Chen, W.Yang**: *An Efficient Driver for Dimmable LED Lighting, IEEE Transactions on Power Electronics*, Volume: 27, Issue: 11, November 2012

[9] **O. Kaplan, F. Issi, M. Ersan**: *A High Efficient Driver Design for LED Lighting System*, 4th International Conference on Power Engineering Energy and Electrical Drives, 2013, Istanbul, Turkey

## Nomenclature

| | |
|---|---|
| $\eta$ | LED lighting lamp efficiency |
| $P_{out}$ | output power |
| $P_{in}$ | input power |
| $THDI$ | total harmonic distortion of current |
| $I_1$ | current of the first harmonic |
| $I_{n,rel}$ | relative value of n-harmonic current in % |

Journal of Energy Technology

JET Volume 10 (2017) p.p. 47-55
Issue 3, October 2017
Type of article 1.01
www.fe.um.si/en/jet.html

# RESEARCH IN THE LABORATORY OF THERMOMECHANICS, APPLIED THERMAL ENERGY, AND NANOTECHNOLOGIES

# RAZISKAVE V LABORATORIJU ZA TERMOMEHANIKO, TERMOENERGETIKO IN NANOTEHNOLOGIJE

Jurij Avsec[✉], Urška Novosel[1]

**Keywords:** thermomechanics, applied thermal energy, nanotechnology

## Abstract

This article presents the research work in the Laboratory of Thermomechanics, Applied Thermal Energy, and Nanotechnologies at the Faculty of Energy Technology of the University of Maribor. The most significant work that has been done is presented.

## Povzetek

Članek predstavlja raziskovalno delo v laboratoriju za termomehaniko, termoenergetiko in nanotehnologije. V članku so predstavljene glavne dejavnosti laboratorija in nekaj pomembnih raziskovalnih dosežkov.

✉ Corresponding author: Corresponding author: Prof. Jurij Avsec, Ph. D., Tel.: +386-7-620-2217, Fax: +386-2-620-2222, Mailing address: Hočevarjev trg 1, 8270 Krško, Slovenia
E-mail address: jurij.avsec@um.si

[1] University of Maribor, Faculty of Energy Technology, Laboratory for Theromechanics, Applied Thermal Energy Technologies and Nanotechnologies, Hočevarjev trg 1, SI-8270 Krško, Slovenia

# 1 THERMAL ANALYSIS AND CALORIMETRY

Among other activities, the Laboratory for Thermomechanics, Applied Thermal Energy Technologies, and Nanotechnologies deals with thermal analysis and calorimetry.

According to *[1],* Thermal Analysis (TA) is the analysis of a change in a sample property (e.g. thermodynamic properties (heat, temperature, mass, enthalpy, etc.), material properties (hardness, susceptibility, etc.), chemical composition or structure) that is related to a specific, imposed temperature alteration. Calorimetry is the measurement of heat.

For the implementation of the above-mentioned analysis, the laboratory has relevant equipment, including a Mettler Toledo TGA/DSC 3+ with the STAR$^e$ system, a Pfeiffer Vacuum Thermostar™ gas analysis system, a Thermo scientific TGA-IR, a Nicolet iS50 FTIR for thermal analysis, and aMettler Toledo EasyMax® 102 for heat flow calorimetry (see Figures 1 and 2).


***Figure 1:*** *Mettler Toledo TGA/DSC 3+ (left), Pfeiffer Vacuum Thermostar™ (right)*


***Figure 2:*** *Thermo scientific TGA-IR and Nicolet iS50 FTIR (left), Mettler Toledo EasyMax 102 (right)*

The Mettler Toledo TGA/DSC 3+ device enables several thermal analysis techniques:

- DTA (Differential Thermal Analysis), in which the temperature difference between the sample and an inert reference substance is measured while being subjected to a temperature alteration, *[1, 2];*
- DSC (Differential Scanning Calorimetry), in which the heat flow in and out of a sample and a reference substance is measured as a function of temperature. With the DSC, exothermic and endothermic effects can be detected, specific heat capacities can be measured, etc., *[2];*
- TGA (Thermogravimetric Analysis), in which the change in the sample mass as a function of temperature is analysed, *[1].* With the TGA, stepwise changes in mass, temperatures that characterize a step in the mass loss, etc, can also be determined, *[2].*

An example of the TGA and DSC curves of the decomposition of Calcium Oxalate Monohydrate ($CaC_2O_4.H_2O$) is shown in Figure 3. Both curves are functions of temperature. Changes in sample mass (in our case mass loss) are shown on the blue curve (TGA curve) as a percentage of the initial sample mass. The violet curve (DSC curve) shows the amount of energy absorbed by the sample (in milliwatts); these are endothermic effects.

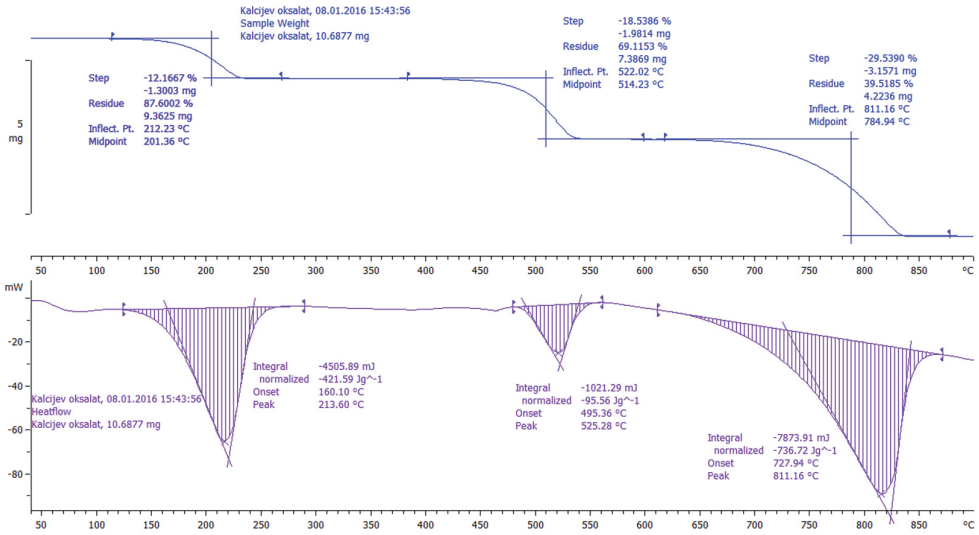


***Figure 3:*** *TGA (above) and DSC (below) curves of the decomposition of Calcium Oxalate Monohydrate*

As can be seen from Figure 3, the TGA is not an identification technique. It cannot identify what the gaseous products that evolved during a TGA measurement are. It can be asserted that the gaseous products with the combination of TGA/DSC with a MS (mass spectrometer) or FTIR (Fourier transform infrared spectrometer). The technique is called EGA (Evolved Gas Analysis), which is the analysis of gases that are evolved from a sample undergoing thermal analysis, *[3].*

However, great care must be taken with the interpretation of results. Time is the parameter common to all instruments (TGA/DSC, MS and FTIR). The data must be correlated mutually.

Mass spectrometry is an extremely sensitive analytical technique for the detection and identification of gaseous substances. The method quantifies atoms or molecules and provides chemical and structural information on the traces of gaseous substances analysed, *[3].*

Fourier transform infrared spectroscopy is a technique in which IR radiation is passed through a sample. It can identify unknown substances, determine the quality of a sample or the amount of components in a substance. FTIR is less sensitive than MS, *[4].*

The Mettler Toledo EasyMax® is a reaction calorimeter for heat flow calorimetry. The heat flow across the reactor wall and quantification of this in relation to the other energy flows inside the reactor is what heat flow calorimetry measures, *[5]*. This technique allows us to measure heat whilst the process temperature is controlled. With the heat flow calorimetry, the heat transfer coefficient, reaction enthalpy, the amount of energy absorbed or released by a chemical reaction, etc. can be determined.

## 2 MEASUREMENTS OF EFFICIENCIES IN BOILERS, HEAT EXCHANGERS, AND HEAT PUMPS

For measurements of efficiency in furnaces, solar collectors, and heat pumps, an entire measuring line must be set up. The heat produced during the measurement is transmitted to a central storage room where heat is then used for heating. Measuring equipment can be used to measure efficiency (energy and exergy efficiency), temperature, and pressure in power systems (see Figures 4 and 5). For the determination of temperature fields, thermovision equipment mounted on drones is also used (Figure 6).

With the measuring system, the following can be measured:

- energy efficiency of boilers, heat pumps, and solar systems,
- exergy efficiency of boilers, heat pumps, and solar systems,
- temperatures in all important points,
- emissions in the case if we test boilers with fossil fuels and biomass.

***Figure 4**: Some details for the thermal part of the laboratory*

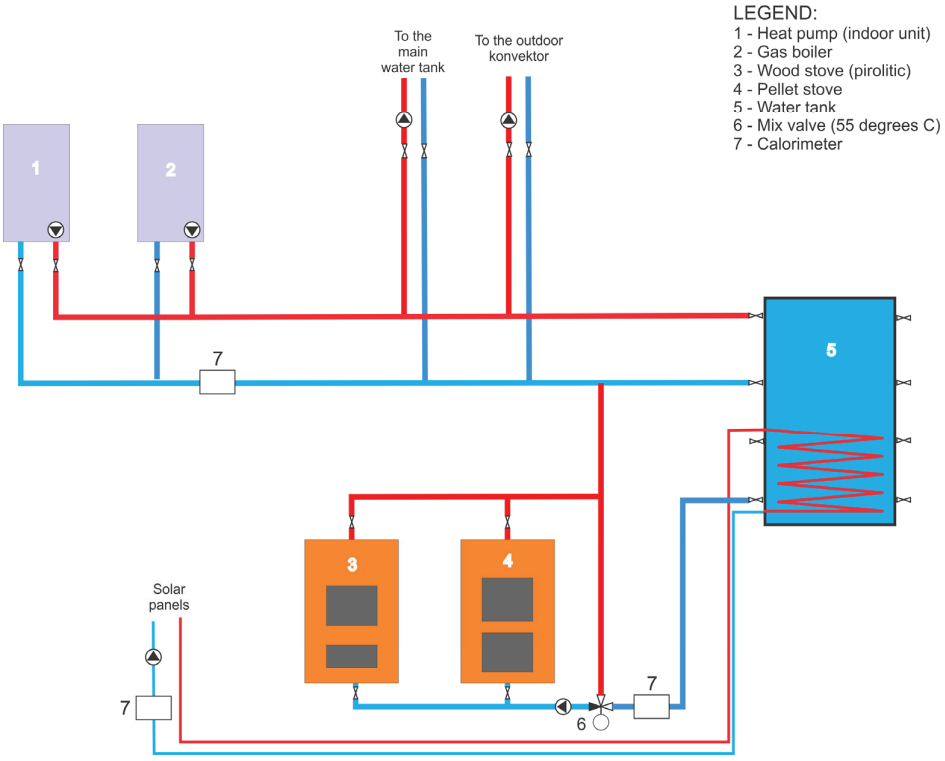


***Figure 5:** Measuring principle line for thermal part of the laboratory*

***Figure 6**: Thermovisional inspections using drones*

## 3 HYDROGEN TECHNOLOGIES

At the laboratory, we are very interested in the development of methanol technologies and hydrogen technologies. The development in this area is carried out in two segments:

1. Hydrogen production. In this field we are developing new hydrogen production systems. We are mainly engaged in the development of hydrogen production from water in connection with a thermoelectric, nuclear power plant or solar thermal power plant. Hydrogen can be obtained from water by means of electrolysis, thermochemical processes, photochemical processes, biochemical processes, and biological processes.

2. Use of hydrogen and methanol. To this end, we are involved in the development and application of fuel cells and hydrogen, Methanol for fuel cell transport will be of vital importance in the future. Normally, fuel cells are divided into groups according to the type of the electrolyte they use. Alkaline fuel cells (AFC) operate optimally within the temperature range of 1200 °C–2500 °C, with concentrated KOH utilized as the electrolyte. A proton exchange membrane fuel cell (PEMFC) uses a very thin polymer membrane as the electrolyte. Its working temperature ranges approximately from 60 °C–80 °C and it currently represents the most promising fuel cell for installation in cars, trains etc. A solid oxide fuel cell (SOFC) uses non-porous metal oxide as the electrolyte. These cells operate at higher temperatures, 600 °C–1000 °C. Also known are phosphoric acid fuel cells (PAFC), and molten carbonate fuel cells (MCFC), but these are not used

very often. At present, all the major automotive factories have their own system of powering vehicles with fuel cells. Due to significant overpopulation and being highly export-oriented, two Japanese factories (Honda and Toyota) have become highly developed in this field. However, other companies and automotive groups are not far behind. On the market today are some transport vehicles, such as the Toyota Mirai and Hyundai IX 35 Fuel cell (Figure 7).


***Figure 7:*** *Hydrogen fuel station with Toyota Mirai car*

## 4 THERMOMECHANICS (MACRO-, MICRO-, AND NANO-LEVELS)

One of the great scientific and technical advancements of the end of 20$^{th}$ and at start of the 21$^{st}$ century was the creation of nanomaterials and nanomechanics. The area that covers all important problems from that field is called, in the broadest sense, “mechanics”. Regarding the cross-sectional diameter, mechanics can be divided into subdisciplines: [6]

macromechanics $10^{-4}$-$10^{-5}$ m,

mesomechanics $10^{-5}$-$10^{-7}$ m,

micromechanics $10^{-7}$-$10^{-8}$ m,

nanomechanics: $10^{-8}$-$10^{-9}$ m.

Since the atomic level (interatomic distance in a crystal lattice) has an order of one to several Å ($10^{-10}$ m), the nanolevel is restricted to $10^{-9}$ m. Accurate data for thermodynamic and transport properties of gases and liquids is crucial for the achievement of many technological goals in thermal and fluid engineering systems. It is estimated that about 50 million pure substances are known today, but with only some 20,000 substances being recorded in journals and manuals. There are approximately 30 thermo-mechanical properties for each pure substance, which are essential to engineering practice (about 12 of which are dependent on pressure and temperature). If the transport properties of every pure substance were measured at ten different temperatures and ten different pressures, then 1,200 measurements would be needed for each

pure substance. Over 100 trillion years of work would be needed to carry out measurement of all properties for every pure substance and known mixtures. Thus, measurements alone are unfeasible and, therefore, analytical methods to determine transport properties are essential. It is possible to determine thermophysical properties by conventional thermodynamics by experimental work or the use of statistical thermodynamics. For the calculation of thermodynamic and transport properties, conventional and statistical thermomechanical methods can be used. The calculated thermophysical properties are used in the further calculation of fluid mechanics, the mechanics of materials, and software to calculate the real behaviour of energy devices.

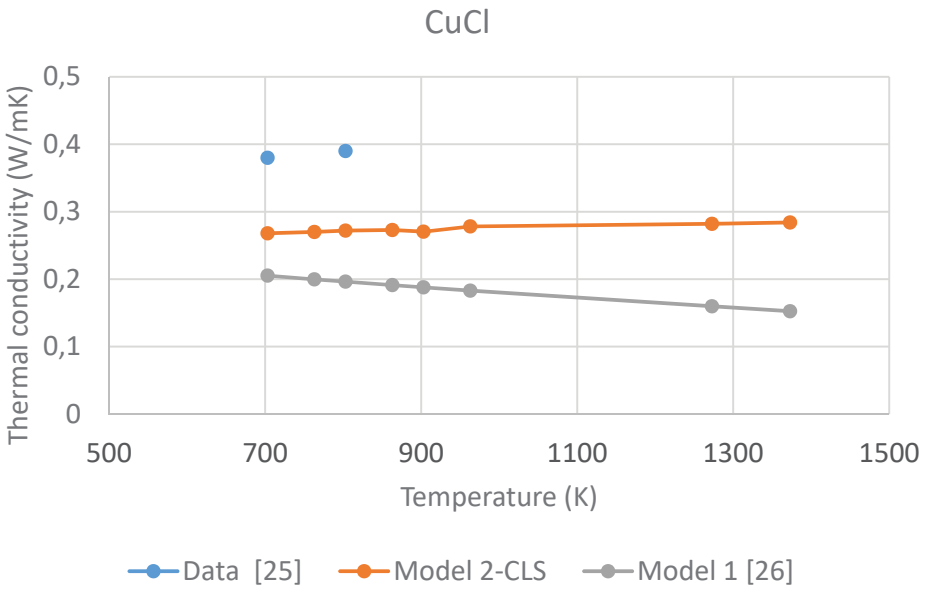


***Figure 8**: Thermal conductivity of molten CuCl, [7]*

## References

[1] **W. Hemminger, S.M. Sarge:** *Handbook of thermal analysis and calorimetry, Principles and practice, edited by M.E. Brown,* Elsevier Science B.V., Vol. 1, Chapter 1. Definitions, nomenclature, terms and literature, 1998

[2] **M. Wagner:** *Thermal Analysis in Practice, Collected Applications,* Mettler Toledo, 2009

[3] **C. Darribère:** *Evolved Gas Analysis, Collected Applications,* Mettler Toledo, 2001

[4] *Introduction to Fourier Transform Infrared Spectroscopy*, Thermo scientific, 2007

[5] **I. Marison, M. Linder, B. Schenker:** *High-sensitive heat-flow calorimetry,* Thermochimica Acta, 310, 43-46, 1998

[6] **J. Avsec, U. Novosel**. The application of nanomechanics in energy technologies =. Journal of energy technology, ISSN 1855-5748. [Tiskana izd.], dec. 2015, vol. 8, iss. 4, str. 23-41

[7] **J Avsec, Z. Wang, G.F. Naterer**, Thermodynamic and transport properties of fluids and solids in a Cu-Cl solar hydrogen cycle. Journal of thermal analysis and calorimetry, ISSN 1388-6150. [Print ed.], jan. 2017, vol. 127, issue 1, pp. 961-967

### Nomenclature

| | |
|---|---|
| ***TA*** | Thermal Analysis |
| ***TGA*** | Thermogravimetric Analysis |
| ***DSC*** | Differential Scanning Calorimetry |
| ***FTIR*** | Fourier Transform InfraRed |
| ***DTA*** | Differential Thermal Analysis |
| ***DSC*** | Differential Scanning Calorimetry |
| ***MS*** | Mass Spectrometer/mass spectrometry |
| ***EGA*** | Evolved Gas Analysis |

Journal of Energy Technology

JET Volume 10 (2017) p.p. 57-69
Issue 3, October 2017
Type of article 1.01
www.fe.um.si/en/jet.html

# ON THE CENTRE-FOCUS PROBLEM IN SOME LIÉNARD SYSTEMS

# O PROBLEMU CENTRA IN FOKUSA V NEKATERIH LIÉNARDOVIH SISTEMIH

Matej Mencinger[1, 2, ℜ]

**Keywords:** Polynomial system of ODEs, Center-focus problem, Complex behavior

## Abstract

A large family of planar systems of ODEs arising from Liénard equations is considered. A Liénard equation $\ddot{x} + f(x)\dot{x} + g(x) = 0$ is commonly used in practical problems, in particular in (electro)mechanics. It is well-known that a Liénard equation can be transformed into an autonomous planar system of ODEs of the form $x' = y - F(x)$, $y' = -g(x)$, where $F'(x) = f(x)$. In this paper $f(x) = 2a_2x + 3a_3x^2 + 4a_4x^3$ and $g(x) = c_1x + c_3x^3 + c_5x^5 + c_7x^7$. In the parameter space $(a_2, a_3, a_4, c_1, c_3, c_5, c_7) \in \mathbb{R}^7$ we consider the center-focus problem and find necessary conditions for the corresponding system having a center at the origin. In the parameter space $(a_2, a_3, a_4, c_1, c_3, c_5, c_7) \in \mathbb{R}^7$ an example with a possible limit cycle and some examples with other complex dynamic behavior are presented.

ℜ Corresponding author: Matej Mencinger, Tel.: +386 2 2294 321, Mailing address: University of Maribor, Faculty of Civil Engineering, Transportation Engineering and Architecture, Smetanova ulica 17, 2000 Maribor, Slovenia. E-mail address: matej.mencinger@um.si

[1] University of Maribor, Faculty of Civil Engineering, Transportation Engineering and Architecture, Smetanova ulica 17, 2000 Maribor, Slovenia.

[2] Institute of Mathematics, Physics and Mechanics, Jadranska 19, 1000, Ljubljana, Slovenia.

## Povzetek

Obravnavana je velika družina ravninskih sistemov navadnih diferencialnih enačb (NDE), ki izhaja iz Liénardove enačbe. Liénardova enačba $\ddot{x} + f(x)\dot{x} + g(x) = 0$ se uporablja v praktičnih problemih, še zlasti v (elektro)mehaniki. Znano je, da se Liénardova enačba lahko preoblikuje v avtonomni ravninski sistem NDE oblike $x' = y - F(x)$, $y' = -g(x)$, kjer je $F'(x) = f(x)$. V tem članku sta $f(x) = 2a_2x + 3a_3x^2 + 4a_4x^3$ in $g(x) = c_1x + c_3x^3 + c_5x^5 + c_7x^7$. V prostoru parametrov $(a_2, a_3, a_4, c_1, c_3, c_5, c_7) \in \mathbb{R}^7$ obravnavamo problem centra in fokusa in poiščemo potrebne pogoje, da ima ustrezen sistem center v izhodišču. Prav tako v prostoru parametrov $(a_2, a_3, a_4, c_1, c_3, c_5, c_7) \in \mathbb{R}^7$ predstavimo primer z možnim limitnim ciklom in nekatere primere z drugimi kompleksnimi dinamičnimi pojavi.

## 1 INTRODUCTION

A great number of mathematical models of physical systems give rise to differential equations of the type

$$\ddot{x} + f(x)\dot{x} + g(x) = 0 \tag{1.1}$$

which is called a Liénard equation. From the mechanical point of view, equation (1.1) can be interpreted as the generalization of the mass-spring-damper system, where $f(x)\dot{x}$ is the damping term and $g(x)$ represents the (nonlinear) spring term. Applications of equation (1.1) can be found in many important examples including chemical reactions, predator-prey models, vibration analysis, etc.

Two famous examples of a Liénard equation are the Van der Pol equation and Duffing's equation. The Van der Pol equation

$$\ddot{x} + \varepsilon(x^2 - 1)\dot{x} + x = 0, \quad \varepsilon > 0$$

describes the circuit of a vacuum tube, whilst Duffing's equation

$$\ddot{x} + \delta\dot{x} + \alpha x + \beta x^3 = \gamma\cos(\omega t),$$

aims to model certain nonlinearly damped/driven oscillators (i.e. a spring pendulum whose spring's stiffness does not exactly obey Hooke's law). Here $x = x(t)$ represents the displacement of the (pendulum) bob at time $t$, $\dot{x}$ represents the first derivative of $x$ with respect to time $t$, and $\ddot{x}$ is the second time-derivative of $x$. Parameters $\alpha, \beta, \gamma, \delta$ and $\omega > 0$ are given (real) constants (case $\beta = \delta = 0$ corresponds to simple harmonic motion).

There are two conventional transitions from homogeneous ODE (1.1) to a planar dynamical system of ODEs. Namely, setting $y = \dot{x}$ we obtain

$$x' = y, \qquad y' = -f(x)y - g(x). \tag{1.2}$$

In (1.1) another approach is possible via the so-called Liénard coordinates. Substituting $y = \dot{x} + F(x)$, where $f(x) = F'(x)$, one obtains

$$x' = y - F(x),\ y' = -g(x). \tag{1.3}$$

Both systems (1.2) and (1.3) are special cases of (continuous) dynamic system called autonomous systems of ODEs, which generally takes the form

$$x' = P(x, y), \qquad y' = Q(x, y). \tag{1.4}$$

Even in planar dynamics, there are several open problems: among them the problem of finding the position and the number of limit cycles bifurcating from a non-hyperbolic singular point, which is a part of famous Hilbert's 16th problem. Most real-life problems are related to the centre-focus problem: this is of distinguishing between a centre, where all orbits in the neighbourhood of the singular point are periodic, and a focus, where all orbits are spiralling away or towards to the singular point/origin (for more details see e.g. *[1]*). Autonomous systems (1.4) cannot contain chaotic dynamics (according to the Poincaré-Bendixon theorem). However, note that Duffing's equation (which is a nonhomogeneous ODE of order two) corresponding to a non-autonomous system $x' = \tilde{P}(x, y, t),\ y' = \tilde{Q}(x, y, t)$) is an example of a dynamical system that exhibits chaotic behaviour. In contrast Duffing's equation is also a classic example of a dynamical system with a limit cycle, *[2,3].* For example, for $f(x) = \varepsilon(x^2 - 1)$ and $g(x) = x$ we obtain

$$x' = y - \varepsilon\left(\frac{x^3}{3} - x\right), \qquad y' = -x$$

which readily contains periodic solutions for $x(t)$ and $y(t)$. In Figs.1-3, there is an example for $\varepsilon = 1.2$ with initial conditions $x(0) = -0.4$, $y(0) = 0.3$. In Fig. 4, the corresponding stream-line plot with a clearly visible limit cycle is presented.

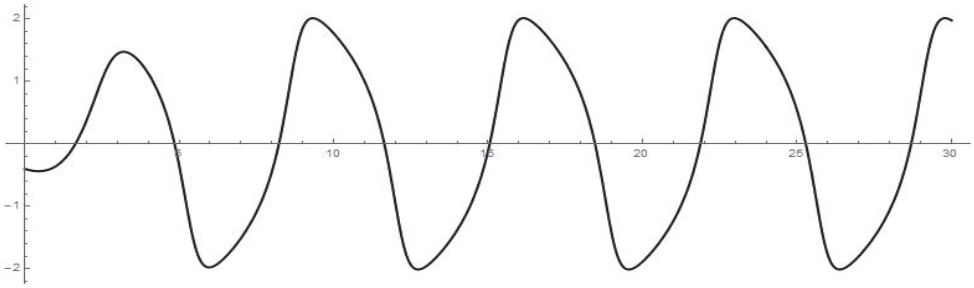


***Figure 1:*** *Initial value solution $x = x(t)$ to Duffing's equation for $\varepsilon = 1.2$; $x(0) = -0.4$, $y(0) = 0.3$*

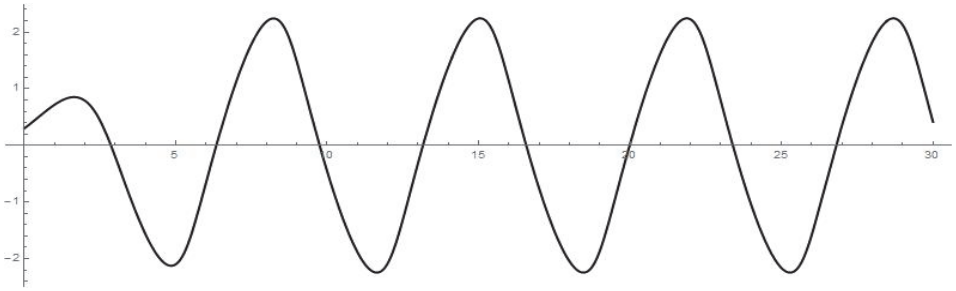


***Figure 2:*** *Initial value solution* $y = y(t)$ *to Duffing's equation:* $\varepsilon = 1.2$*;* $x(0) = -0.4$*,* $y(0) = 0.3$

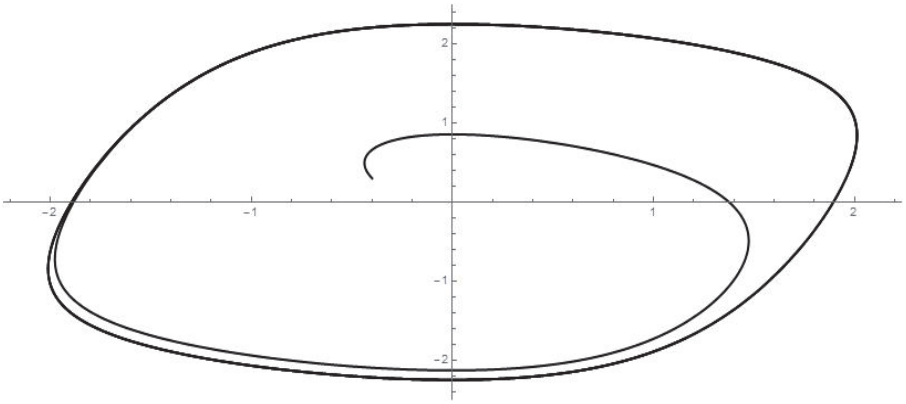


***Figure 3:*** *A solution tending to limit cycle of Duffing's equation:* $\varepsilon = 1.2$ *and* $x(0) = -0.4$*,* $y(0) = 0.3$

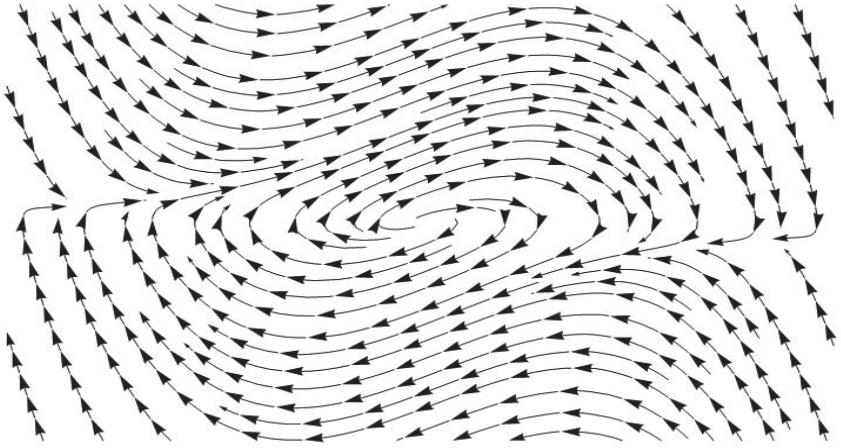

***Figure 4:*** *Streamline-plot (Mathematica) of Duffing's equation for* $\varepsilon = 1.2$ *containing a limit cycle*

Usually for systems (1.4) and, consequently, also for systems (1.2) and (1.3) singular points $\vec{x}_0$ are hyperbolic; this means that no eigenvalue of the Jacobian matrix

$$J(\vec{x}_0) = \begin{bmatrix} \frac{\partial P}{\partial x} & \frac{\partial P}{\partial y} \\ \frac{\partial Q}{\partial x} & \frac{\partial Q}{\partial y} \end{bmatrix}, \text{ where } \vec{x} = (x, y)$$

evaluated at $\vec{x}_0$ has the real part equal to zero. In this case the linearized system $\vec{x}' = J(\vec{x}_0)$ may (locally – near singular point $\vec{x}_0 = (x_0, y_0)$) be used to approximate the original system (1.4). More precisely, the approximation is in terms of a continuous invertible map, which locally (near singularity) takes parametrized solutions of the linearized system $\vec{x}' = J(\vec{x}_0)$ to the parametrized solutions of the original system (1.4). This is the statement of the Hartman—Grobman theorem *[4]*. For any singular point $\vec{x}_0$ of system (1.4) one of the following five »generic cases«, according to the Jordan canonical form of $J(\vec{x}_0)$, appears

$$(i)\begin{bmatrix} \lambda_1 & 0 \\ 0 & \lambda_2 \end{bmatrix}, \lambda_{1,2} \neq 0 \ \ (ii)\begin{bmatrix} 0 & \omega \\ -\omega & 0 \end{bmatrix}, (iii)\begin{bmatrix} \omega & 0 \\ 0 & 0 \end{bmatrix}, (iv)\begin{bmatrix} 0 & \omega \\ 0 & 0 \end{bmatrix}, \omega \neq 0 \ \ (v)\begin{bmatrix} 0 & 0 \\ 0 & 0 \end{bmatrix}.$$

None, except the first one, are within the scope of the Hartman—Grobman theorem (for any $\omega \neq 0$) and must be considered case by case/separately. Systems corresponding to the Jacobian matrix of the form $(ii)$ are the most studied planar systems. The addition of nonlinear terms may result either in centre or in focus. In this paper, we will consider a special case of (1.2) of the form

$$x' = y, \qquad y' = -(2a_2x + 3a_3x^2 + 4a_4x^3)y - (c_1x + c_3x^3 + c_5x^5 + c_7x^7), \qquad (1.5)$$

where $a_2, a_3, a_4, c_1, c_3, c_5, c_7 \in \mathbb{R}$, and analyse the stability for the whole family (1.5).

## 2 THE ANALYSIS OF SYSTEM (1.5)

### 2.1 Case $c_1 > 0$

If $c_1 > 0$ introducing new coordinates $X = c_1x, Y = c_1y$ one can obtain system $X' = Y$, $Y' = -(2a_2X + 3a_3X^2 + 4a_4X^3)Y - (X + c_3X^3 + c_5X^5 + c_7X^7)$. The corresponding Jacobian at singular point (0,0) is

$$J(0,0) = \begin{bmatrix} 0 & 1 \\ -1 & 0 \end{bmatrix}$$

which yields a centre or focus at the origin. In Fig. 5 there is a stream-line plot of a centre.

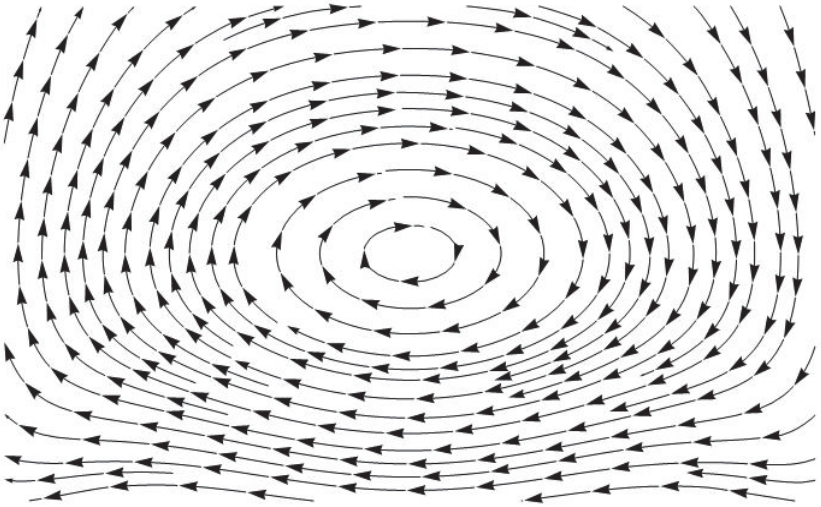

***Figure 5:*** *Centre for system (5), with* $a_2 = a_3 = 0,\ a_4 = \frac{3}{4}, c_1 = 1, c_3 = c_5 = 0, c_7 = 2$

Note that the complete analysis of case $c_1 > 0$ is done in a separate section in the sequel; it will be seen that $a_3 = 0$ is the sufficient condition to obtain a centre in system (1.5). However, distinguishing between a centre and a focus just from a streamline plot (e.g. in Mathematica) is impossible and much too inaccurate (since the stream-plot of a focus is too similar to the stream-plot of a centre). In the case of a focus, it is much more convenient to consider a single solution, like in Figs. 6-7 in which graphs of $x = x(t)$ and $y = y(t)$ are shown. In Fig. 8, the parametric solution $(x(t), y(t))$ is shown in the phase plane $(x, y)$.

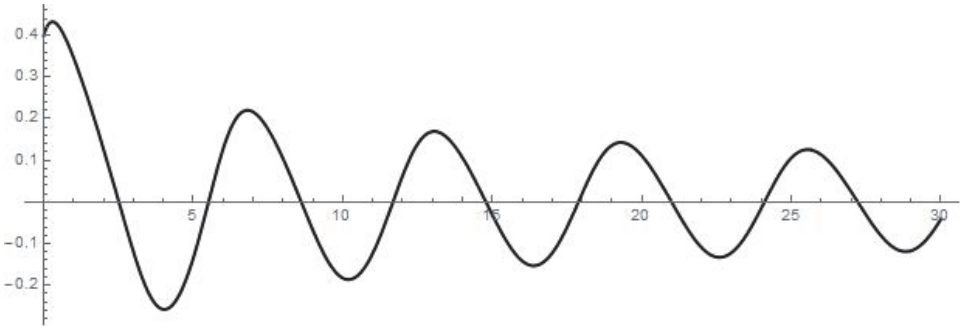


***Figure 6:*** *Particular solution* $x = x(t)$ *of (1.5) with* $a_2 = a_4 = 0,\ a_3 = c_1 = 1, c_3 = 2, c_5 = c_7 = 0$

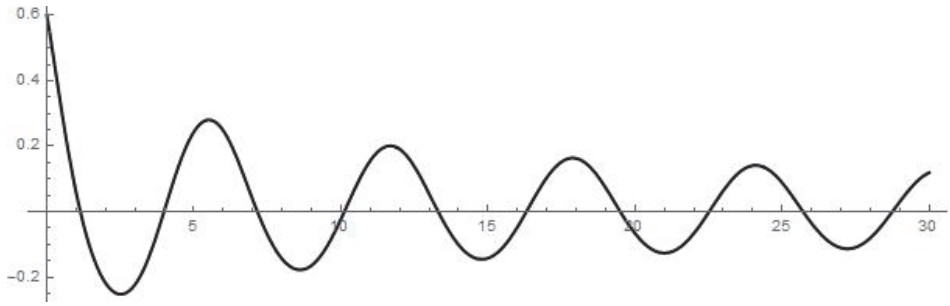


***Figure 7:*** *Particular solution* $y = y(t)$ *of (1.5) with* $a_2 = a_4 = 0,\ a_3 = c_1 = 1, c_3 = 2, c_5 = c_7 = 0$

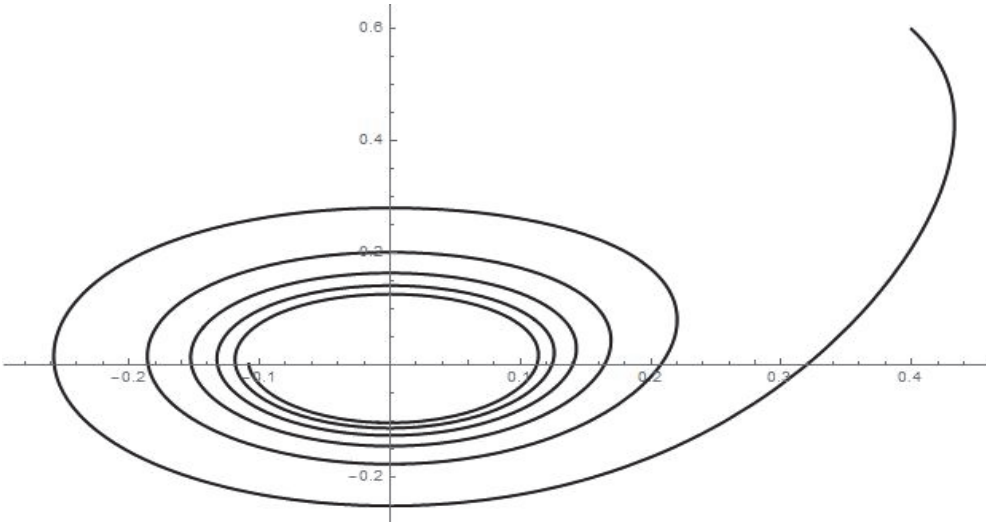


**Figure 8:** Trajectory $(x(t), y(t))$ of (1.5) with $a_2 = a_4 = 0,\ a_3 = 1, c_1 = 1, c_3 = 2, c_5 = c_7 = 0$

## 2.2 Case $c_1 < 0$

If $c_1 < 0$ introducing new coordinates $X = c_1 x, Y = c_1 y$ one yields $X' = Y,\ Y' = -(2a_2 X + 3a_3 X^2 + 4a_4 X^3)Y - (-X + c_3 X^3 + c_5 X^5 + c_7 X^7)$. The corresponding Jacobian matrix at a singular point $(0,0)$ is

$$J(0,0) = \begin{bmatrix} 0 & 1 \\ 1 & 0 \end{bmatrix}.$$

The eigenvalues of $J(0,0)$ are $\lambda_{1,2} = \pm 1$, yielding a hyperbolic singular point: a saddle with an unstable singularity. The dynamics near the origin (according to the Hartman−Grobman theorem) are topologically conjugate to the linear system $X' = Y,\ Y' = X$ (see Fig. 9), and no further analysis is needed in this case.

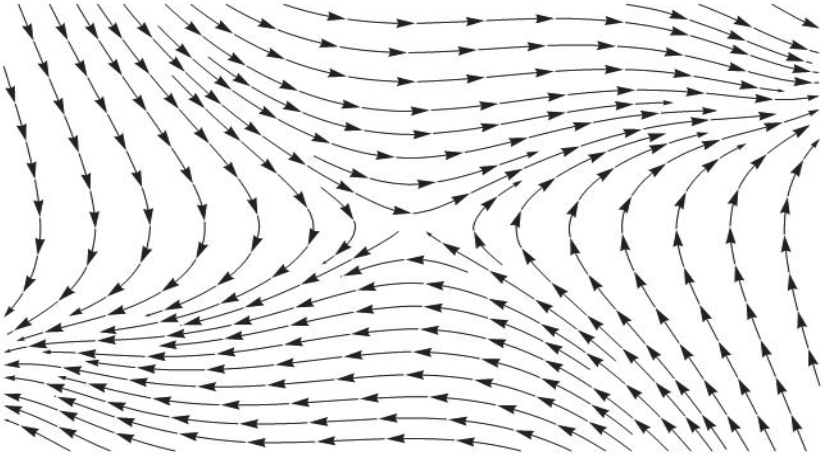

***Figure 9:*** *Phase portrait of a saddle for (1.5);* $a_2 = a_4 = 0,\ a_3 = 1, c_1 = -1, c_3 = c_5 = 0, c_7 = 1$

### 2.3 Case $c_1 = 0$

If $c_1 = 0$, the system takes the form $x' = y,\ y' = -(2a_2x + 3a_3x^2 + 4a_4x^3)y - (c_3x^3 + c_5x^5 + c_7x^7)$, and $(0,0)$ is a non-elementary (nilpotent) singular point if type $(iv)$, since the corresponding Jacobian at singular point $(0,0)$ is

$$J(0,0) = \begin{bmatrix} 0 & 1 \\ 0 & 0 \end{bmatrix}.$$

The blow-up desingularization gives rise to the type of stability in this case (see *[5,6]* for details). Note that the case $(v)$ can never appear for Lienard systems since $\frac{\partial P}{\partial y} = 1 \neq 0$.

## 3 THE CENTRE-FOCUS ANALYSIS

In order to consider the centre-focus problem, we briefly recall an approach *[1]* for studying the problem for planar polynomial systems (1.4), where $P(x,y) = y + h.o.t.$ and $Q(x,y) = -x + h.o.t.$ Here $h.o.t.$ stands for $\sum_{i+j=2}^{n} P_{i,j}x^iy^j$, and $\sum_{i+j=2}^{n} Q_{i,j}x^iy^j$, respectively. Note that via the (reverse) time transformation $\tau = -t$ this is equivalent to $P(x,y) = y + h.o.t.$ and $Q(x,y) = -x + h.o.t.$, therefore we make no difference between these two cases. Here $P(x,y)$ and $Q(x,y)$ are polynomials of degree at most $n$ without constant and linear terms. It is convenient to introduce the polar coordinates $u = r\cos\varphi, v = r\sin\varphi$ and consider the so-called Poincaré return map $R(r)$. Introducing the polar coordinates into (1.4) with $P(x,y) = y + h.o.t.$ and $Q(x,y) = -x + h.o.t.$ yields the equation of the trajectories

$$\frac{dr}{d\varphi} = \frac{r^2F(r,\cos\varphi,\sin\varphi)}{1 + rG(r,,\cos\varphi,\sin\varphi)} = R(r,\varphi).$$

Obviously, $r = 0$ is a solution to $\frac{dr}{d\varphi} = R(r, \varphi)$, since $R(0, \varphi) \equiv 0$. The function $R(r, \varphi)$ is periodic (with the least period $2\pi$ in variable $\varphi$) and analytic for (small enough) $|r| \leq r^*$ (and all $\varphi$). Thus, $R(r, \varphi)$ can be expanded in a convergent power series in $r$ to obtain

$$\frac{dr}{d\varphi} = \mathrm{r}^2 R_2(\varphi) + \mathrm{r}^3 R_3(\varphi) + \cdots \tag{3.1}$$

The continuous dependence on the initial conditions and the fact that $r = 0$ is a solution for all $\varphi \in [0,2\pi]$ yield that every solution to the above equation in a sufficiently small neighbourhood of the origin intersects every ray $\varphi$=$\varphi_0$, $\varphi_0 \in [0,2\pi]$. This means that without loss of generality one can choose the line segment $\Sigma = \{(u, v);\ v = 0, 0 \leq u \leq r^*\}$, where $r^*$ is chosen to be small enough.

Next, we consider the solution of (3.1) with the initial condition $r(\varphi = 0) = r_0$ and expand it into a power series in $r_0$ to obtain

$$r(\varphi, r_0) = w_1(\varphi) r_0 + w_2(\varphi) r_0^2 + w_3(\varphi) r_0^3 + \cdots \tag{3.2}$$

which is also convergent for all $\varphi \in [0,2\pi]$ and all $|r_0| \leq r^*$. The $r(\varphi)$ from (3.2) is a solution of (3.1) and inserting $r(\varphi, r_0)$ into (3.2) yields recurrence differential equations for functions $w_j(\varphi)$ (see *[1]* for more details). We consider one revolution of $r = r(\varphi, r_0)$ beginning on $r_0 \in \Sigma$ where $\varphi$ is assumed to be $0$ and study the return to $\Sigma$ (which occurs at $\varphi = 2\pi$, that is, after one revolution). Thus, the Poincaré return map $R(r)$ is defined by

$$\mathcal{R}(r_0) = r(2\pi, r_0) = r_0 + w_2(2\pi) r_0^2 + w_3(2\pi) r_0^3 + \cdots$$

The coefficients $\eta_j := w_j(2\pi)$ for $j > 1$, defined in the above equation are called *Lyapunov numbers.*

From the definition of polar coordinates, we readily conclude that the zeros of the difference function $\mathcal{R}(r_0) - r_0$ correspond to closed orbits. In particular, isolated zeros correspond to limit cycles, and if $\mathcal{R}(r_0) - r_0 \equiv 0$, the system has a centre at the origin, which means that for all $j > 1$ the Lyapunov numbers $\eta_j$ must vanish.

However, computing Lyapunov numbers requires the integration of trigonometric functions, which can be very difficult problems for some cases. Poincare and Lyapunov proved that system (1.4) with $P(x, y) = y + h.o.t.$ and $Q(x, y) = -x + h.o.t.$ has centre at the origin if it admits the first integral of the form

$$\Phi(x, y) = x^2 + y^2 + \sum_{i+j \geq 3} v_{ij} x^i y^j, \tag{3.3}$$

which is an analytic function in a neighbourhood of the origin $(0,0)$. By definition, $\Phi$ is a first integral of system (1.4) if $\Phi$ is a solution to the following PDE

$$\Psi := \frac{\partial \Phi(x, y)}{\partial x} \cdot P(x, y) + \frac{\partial \Phi(x, y)}{\partial y} Q(x, y) \equiv 0. \tag{3.4}$$

In agreement with formula (3.4), equation $\Psi \equiv 0$ can be solved only on some special variety (set of zeros) in the (affine) space of parameters $a_{ij}, b_{ij}$ defined by coefficients of $P(x, y)$ and $Q(x, y)$. Generally, from (3.4) using step-by-step process of equating the proper coefficients of $\Psi$ to zero we obtain

$$\Psi = g_4(a_{ij}, b_{ij})(x^2 + y^2)^2 + g_6(a_{ij}, b_{ij})(x^2 + y^2)^3 + g_8(a_{ij}, b_{ij})(x^2 + y^2)^4 + \cdots$$

yielding $\Psi \equiv 0$ if and only if

$$g_4(a_{ij}, b_{ij}) = g_6(a_{ij}, b_{ij}) = \cdots = g_{2k}(a_{ij}, b_{ij}) = \cdots = 0 \tag{3.5}$$

for all $k \geq 2$. The numbers (polynomials) $g_{2k}(a_{ij}, b_{ij})$ are called *focus quantities [1]*. Finally, the centre-focus problem reduces to find the conditions for vanishing all focus quantities $g_{2k}(a_{ij}, b_{ij})$.

For case (1.5), we computed the first several polynomials $g_{2k}(a_{ij}, b_{ij})$ using and obtained

$g_4 = -\frac{3a_3}{4}$,

$g_6 = \frac{a_3}{32}(76a_2^2 + 21c_3)$,

$g_8 = -\frac{a_3}{3072}(33834a_2^4 + 19736a_2^2c_3 + 9(133a_3^2 + 229c_3^2 - 216c_5) - 15728a_2a_4)$,

$g_{10} = \frac{a_3}{184320}(15467244a_2^6 - 11734288a_2^3a_4 + 10684399a_2^4c_3 - 2776152a_2a_4c_3 - 3a_2^2(484752a_3^2 - 789569c_3^2 + 559144c_5) - 3a_2^2(484752a_3^2 - 789569c_3^2 + 559144c_5) + 9(52064a_4^2 + 5(4929a_3^2c_3 + 2901c_3^3 - 6164c_3c_5 + 2568c_7)))$, etc.

The expressions for the other focus quantities are too long to be presented here, but can easily be computed using Mathematica or any other appropriate computer algebra system. Obviously, the condition $a_3 = 0$ is necessary for (3.5), since $a_3$ is a cofactor of $g_{2k}(a_{ij}, b_{ij})$ for any $k$.

This means that system (1.5) for $a_3 = 0$ and $c_1 > 0$ has centre at the origin for arbitrary $a_2, a_4, c_3, c_5, c_7 \in \mathbb{R}$ and the phase portrait in the neighbourhood of the origin is topologically equivalent to the phase portrait shown in Fig. 5.

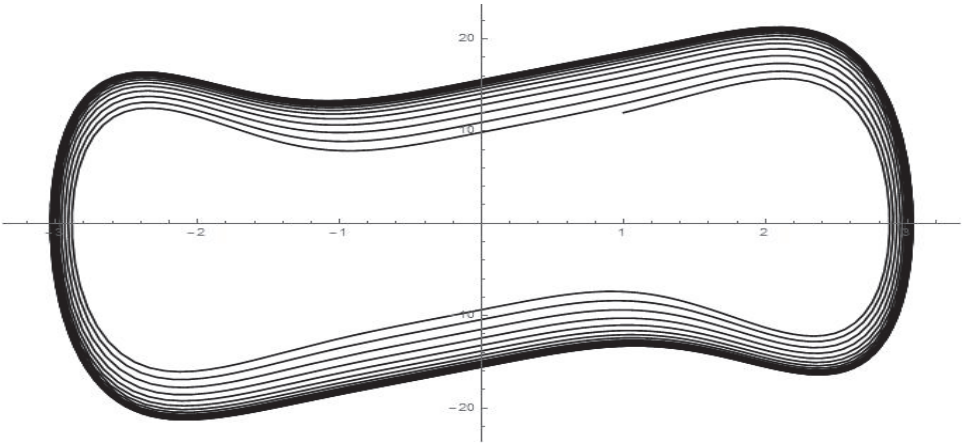


***Figure 10:*** *A non-trivial limit cycle for (1.2) of the form* $x' = y, y' = -(x^2 - 3)y - 5x^3(x^2 - 5)$

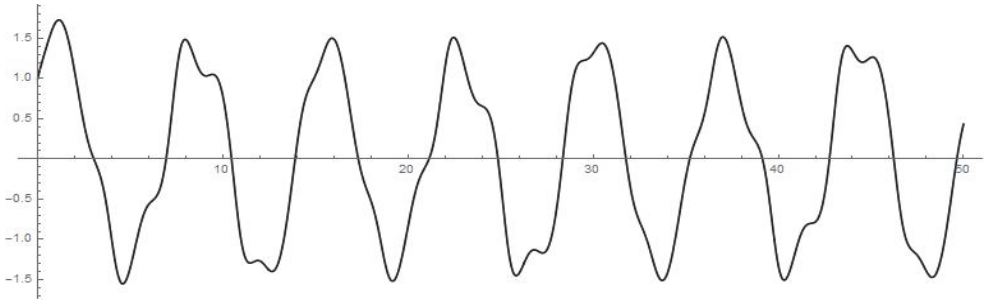


***Figure 11:*** *Complex dynamics of* $x' = y, y' = (\frac{1}{2} - x^2)y - \frac{x^3(x^2-4)}{16} - x + 2\sin 3t$: $x = x(t)$

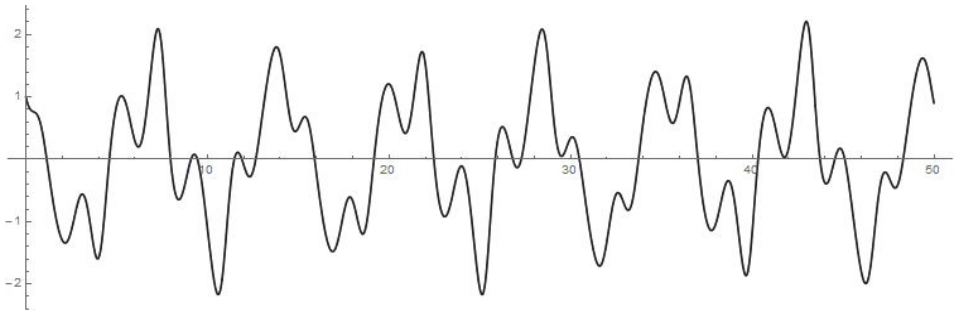


***Figure 12:*** *Complex dynamics of* $x' = y, y' = (\frac{1}{2} - x^2)y - \frac{x^3(x^2-4)}{16} - x + 2\sin 3t$: $y = y(t)$

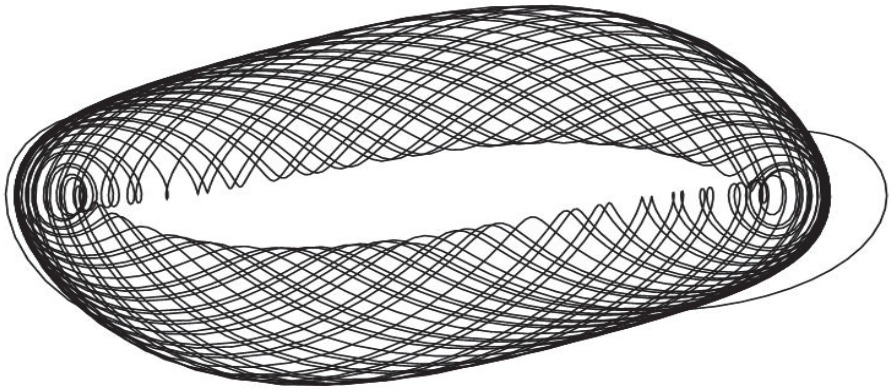

***Figure 13:*** *Complex dynamics of* $x' = y, y' = (\frac{1}{2} - x^2)y - \frac{x^3(x^2-4)}{16} - x + 2\sin 3t$: $(x(t), y(t))$

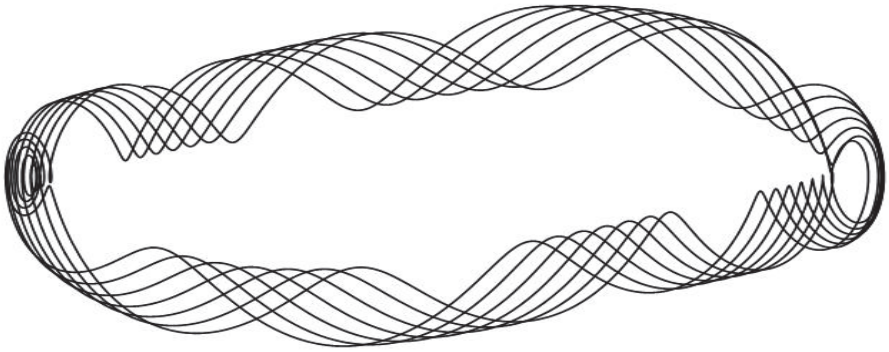

***Figure 14:*** *Complex dynamics of* $x' = y, y' = (\frac{1}{2} - x^2)y - \frac{x^3(x^2-4)}{16} - x - 3\sin 7t$: $(x(t), y(t))$

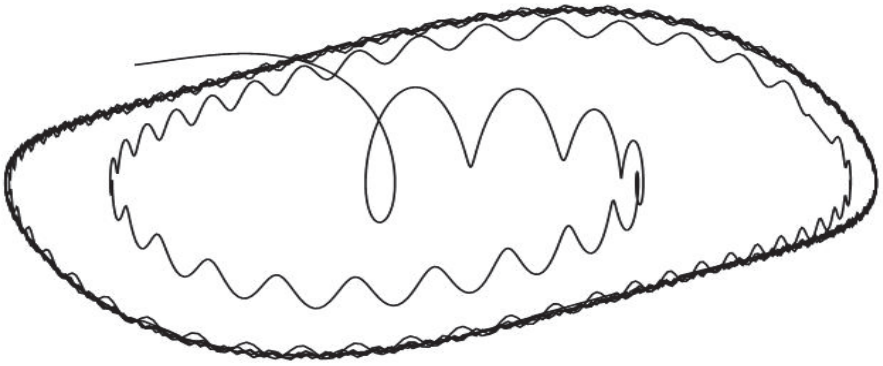

***Figure 15:*** *A single trajectory of* $x' = y, y' = (\frac{1}{2} - x^2)y - \frac{x^3(x^2-4)}{16} - x - 3\sin 2t^2$: $(x(t), y(t))$

## 4 CONCLUSIONS

The centre-focus problem for system (1.5) is solved for necessary conditions. It is proven that the crucial parameter that distinguishes between the centre and focus in (1.5) is $a_3$. The condition $a_3 \neq 0$ yields focus, while $a_3 = 0$ defines a centre for any choice of other parameters. Note also that there are many nontrivial examples of system (1.2) that probably admit limit cycles, for example system $x' = y, y' = -(x^2 - 3)y - 5x^3(x^2 - 5))$ shown in Fig.10. According to the well-known Liénard theorem, *[3]*, system (1.2) admits a unique stable limit cycle if $f$ and $g$ are continuously differentiable, $g$ is odd and $g(x) > 0$ for $x > 0$, $f$ is an even function and $\int_0^x f(u)\,du < 0$ for $0 < x < a$, and $\int_0^x f(u)\,du > 0$ and increasing for $x > a$; for some $a \in \mathbb{R}_+$.

Finally, note that a non-autonomous modification of system (1.2): $x' = y,\ y' = -f(x)y - g(x) + h(t)$ may exhibit other complex dynamics, as shown in Figs. 11-15.

## References

[1] **V.G. Romanovski, D.S. Shafer:** *The Center and Cyclicity Problems: A Computational Algebra Approac,* Birkhäuser, Boston, 2009

[2] **A. Constantin:** On the Oscillation of Solutions of the *Liénard Equation,* J. Math. Ann. Appl., Vol. 205, p.p. 207-215, 1997

[3] **A. Palit, D.P. Datta:** *On a Finite Number of Limit Cycles in a Liénard System*, Int. J. Pure and Applied Math., Vol. 59, p.p. 469-488, 2010

[4] **N. Li, M. Han, V.G. Romanovski:** Cyclicity of some Liénard Systems, Commun. Pure Appl. Anal. Vol. 14, p.p. 2127-2150, 2015

[5] **F. Dumortier, J. Llibre, J. C. Artes:** *Qualitative Theory of Planar Differential Systems*, Springer-Verlag, Berlin Heidelberg, 2006

[6] **M. Jesús Álvares, A. Ferragut, X. Jarque:** A survey on the blow up technique, Internat. J. Bifur. Chaos Appl. Sci. Engrg. Vol. 21, p.p. 3103, 2011

Journal of Energy Technology

Author instructions

www.fe.um.si/en/jet.html

# MAIN TITLE OF THE PAPER
# SLOVENIAN TITLE

*Author[1], Author [2], Corresponding author*ℜ

Keywords: (Up to 10 keywords)

## Abstract

Abstract should be up to 500 words long, with no pictures, photos, equations, tables, only text.

## Povzetek

(Abstract in Slovenian language)

Submission of Manuscripts: All manuscripts must be submitted in English by e-mail to the editorial office at jet@um.si to ensure fast processing. Instructions for authors are also available online at http://www.fe.um.si/en/jet/author-instructions.html.

Preparation of manuscripts: Manuscripts must be typed in English in prescribed journal form (MS Word editor). A MS Word template is available at the Journal Home page.

A title page consists of the main title in the English and Slovenian language; the author(s) name(s) as well as the address, affiliation, E-mail address, telephone and fax numbers of author(s). Corresponding author must be indicated.

Main title: should be centred and written with capital letters (ARIAL bold 18 pt), in first paragraph in English language, in second paragraph in Slovenian language.

Key words: A list of 3 up to 6 key words is essential for indexing purposes. (CALIBRI 10pt)

Abstract: Abstract should be up to 500 words long, with no pictures, photos, equations, tables, - text only.

Povzetek: - Abstract in Slovenian language.

Main text should be structured logically in chapters, sections and sub-sections. Type of letters is Calibri, 10pt, full justified.

ℜ Corresponding author: Title, Name and Surname, Organisation, Department, Address, Tel.: +XXX x xxx xxx, E-mail address: x.x@xxx.xx

[1] Organisation, Department, Address

[2] Organisation, Department, Address

Units and abbreviations: Required are SI units. Abbreviations must be given in text when first mentioned.

Proofreading: The proof will be send by e-mail to the corresponding author in MS Word's Track changes function. Corresponding author is required to make their proof corrections with accepting or rejecting the tracked changes in document and answer all open comments of proof reader. The corresponding author is responsible to introduce corrections of data in the paper. The Editors are not responsible for damage or loss of submitted text. Contributors are advised to keep copies of their texts, illustrations and all other materials.

The statements, opinions and data contained in this publication are solely those of the individual authors and not of the publisher and the Editors. Neither the publisher nor the Editors can accept any legal responsibility for errors that could appear during the process.

Copyright: Submissions of a publication article implies transfer of the copyright from the author(s) to the publisher upon acceptance of the paper. Accepted papers become the permanent property of "Journal of Energy Technology". All articles published in this journal are protected by copyright, which covers the exclusive rights to reproduce and distribute the article as well as all translation rights. No material can be published without written permission of the publisher.

Chapter examples:

# 1 MAIN CHAPTER

**(Arial bold, 12pt, after paragraph 6pt space)**

## 1.1 Section

**(Arial bold, 11pt, after paragraph 6pt space)**

### 1.1.1 Sub-section

**(Arial bold, 10pt, after paragraph 6pt space)**

Example of Equation (lined 2 cm from left margin, equation number in normal brackets (section. equation number), lined right margin, paragraph space 6pt before in after line):

Equation (1.1)

Tables should have a legend that includes the title of the table at the top of the table. Each table should be cited in the text.

Table legend example:

***Table 1:*** *Name of the table (centred, on top of the table)*

Figures and images should be labelled sequentially numbered (Arabic numbers) and cited in the text – Fig.1 or Figure 1. The legend should be below the image, picture, photo or drawing.

Figure legend example:

***Figure 1:*** *Name of the figure (centred, on bottom of figure, photo, or drawing)*

## References

[1] **N. Surname:** *Title,* Journal Title, Vol., Iss., p.p., Year of Publication

[2] **N. Surname:** *Title,* Publisher, Year of Publication

[3] **N. Surname:** *Title* [online], Publisher or Journal Title, Vol., Iss., p.p., Year of Publication. Available: website (date accessed)

Examples:

[1] **J. Usenik**: *Mathematical model of the power supply system control*, Journal of Energy Technology, Vol. 2, Iss. 3, p.p. 29 – 46, 2009

[2] **J. J. DiStefano, A.R. Stubberud, I. J. Williams**: *Theory and Problems of Feedback and Control Systems*, McGraw-Hill Book Company, 1987

[3] **T. Žagar, L. Kegel:** *Preparation of National programme for SF and RW management taking into account the possible future evolution of ERDO* [online], Journal of Energy Technology, Vol. 9, Iss. 1, p.p. 39 – 50, 2016. Available: http://www.fe.um.si/images/jet /Volume 9_Issue1/03-JET_marec_2016-PREPARATION_OF_NATIONAL.pdf (7. 10. 2016)

Example of reference-1 citation: In text *[1],* text continue.

**Nomenclature**

| **(Symbols)** | (Symbol meaning) |
|---|---|
| ***t*** | time |


JET

JET I Journal of Energy Technology I Vol. 10, Issue 3, October 2017 I University of Maribor, Faculty of Energy Technology

ISSN 1855-5748

9 771855 574008